FACULTY OF SCIENCE
UNIVERSITY OF COPENHAGEN

Master thesis in geophysics June 26, 2009

Seasonality over Greenland during the Holocene and possible explanations of the 8.2 kyr event

A study based on the circulation model ECBilt-CLIO

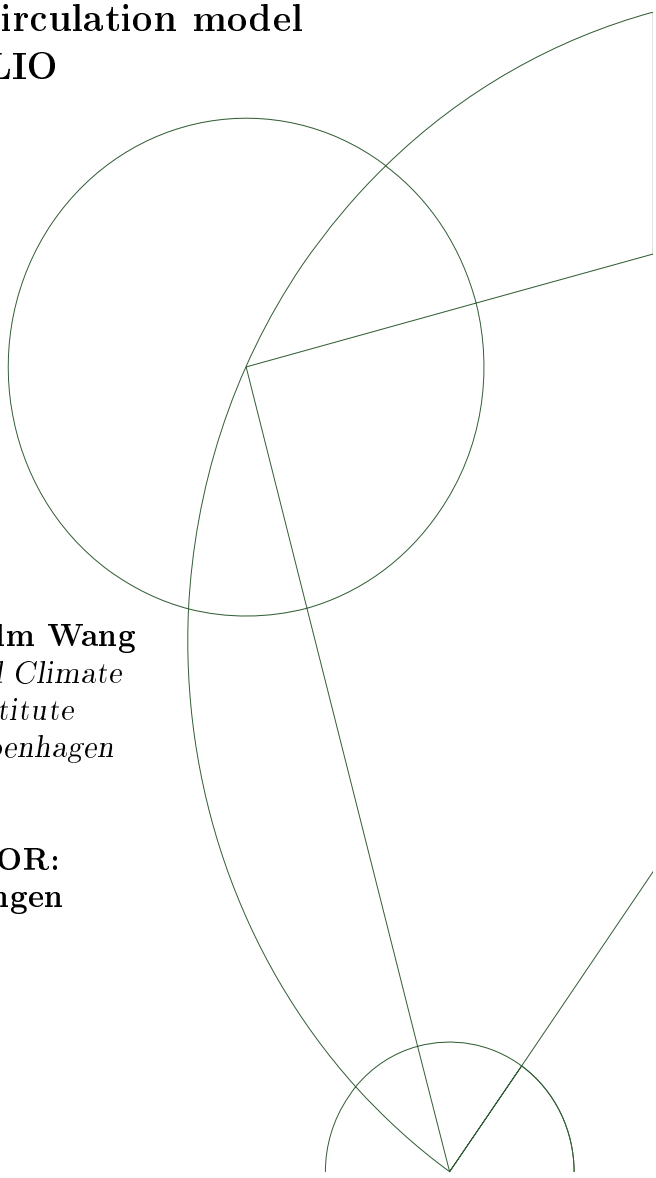

Peter Riddersholm Wang
Centre for Ice and Climate
Niels Bohr Institute
University of Copenhagen

SUPERVISOR:
Peter L. Langen

Abstract

Using an Earth Model of Intermediate Complexity, experiments are performed during the Holocene to study a) the seasonality of precipitation in Greenland and the effect on the interpretation of ice-core signals, and b) possible mechanisms that can account for the sudden decrease in temperature seen in ice cores from Greenland 8.2 kyr ago.

a) Throughout the Holocene orbital parameters have changed resulting in a 5 W/m^2 drop and a 0.9 W/m^2 rise in annually averaged insolation at 80 and 20°N, respectively. It has been speculated that this increase in the meridional gradient of the annual mean solar forcing can lead to changes in the seasonality of Greenland precipitation. The isotope signal in ice cores are precipitation weighted, meaning that a signal is only recorded when it snows, and a change in the seasonality of precipitation will thus cause a bias in the signal. If, for instance, the amount of summer precipitation drops, this will appear as a cooling in the signal, even if the temperature is constant.

b) δO^{18} records from Greenland ice cores show a large excursion of $\sim 2‰$, found at 8.2 kyr ago. This cooling has been detected in many other indicators in the Greenland ice cores, and in cores from many other locations, indicating that the 8.2 kyr event was not restricted to the North Atlantic region. It is believed, that the event is caused by freshwater discharges, originating from the melting of the Laurentide ice sheet.

Orbital and freshwater forcings are built into the model, and the results will give an indication of the effects on regional and global climate.

Resume

Ved at benytte en såkaldt Earth Model of Intermediate Complexity, vil eksperimenter gennem Holocæn blive udført for at studere a) ændringer i sæsonaliteten af nedbør i Grønland samt effekterne dette kan have når man skal fortolke signalerne i iskerner, og b) mulige mekanismer der kan forklare den pludselige nedkøling observeret i iskerner fra Grønland 8.200 år før nu.

a) Jordens baneparametre har ændret sig gennem Holocæn, og solindstrålingen ved 80 og 20° nordlig bredde er hhv. faldet 5 W/m^2 og øget 0.9 W/m^2. Det er blevet foreslået, at denne forøgelse af den meridionale gradient kan føre til ændringer i sæsonaliteten af nedbør i Grønland. Da isotop signaler i iskerner er nedbørs-vægtede, dvs. et signal kun bliver optaget når det sner, vil en ændring i sæsonaliteten af nedbør føre til forskydelser af signalet. For eksempel vil et fald i mængden af sommernedbør give sig til udtryk i et temperaturfald i signalet, selvom temperaturen er konstant.

b) δO^{18} målinger fra iskerner i Grønland viser store udsving på $\sim 2‰$ for 8.200 år siden. Denne nedkøling er blevet observeret i mange andre indikatorer i Grønlandske iskerner samt mange andre steder på kloden, hvilket indikerer at begivenheden var et globalt fænomen. Forklaringen skal sansynligvis findes i udledningen af ferskvand i det nordlige Atlanterhav, der stammer fra afsmeltning fra Laurentide iskappen.

Orbital- og ferskvand-forceringer er inkorporeret i modellen, og resultaterne vil give en indikation af effekterne af disse på det regionale og globale klima.

Contents

Chapter 1

Introduction

Climate usually refers to the average weather conditions, including temperature, humidity, precipitation, wind, pressure etc., over a period of time for a given area. Since the weather influences the life on our planet, changes in global or regional climate is something that affect all activities on the Earth, and man has striven for an understanding of the mechanisms causing climate change throughout the modern era.

Studies during the last few decades have shown that climate change is most likely caused by various natural and anthropogenic factors such as variations in solar radiation, changes in ocean circulation, vegetation type and density and changes in greenhouse gases (GHG) and aerosols (IPCC, 2007). The interaction between the different factors is complex and not easily understood.

Focusing on the Atlantic thermohaline circulation (THC), it is defined by Wunsch (2002) as the ocean circulation of its mass, including warm, saline surface water flowing northward and cold, dense water flowing southward in depth. One of the main features of the THC is the redistribution of heat from low to high latitudes, and if this overturning circulation is changed the global and regional climate is affected in various ways (Pedlosky, 1998).

Observations of the climate have only been carried out in the modern era, and proxies for past climate change, including sediment and ice cores, tree rings and coral, are used to study past climate change. Especially ice cores from Greenland and Antarctica have proven to be an important source of information on Earth's climate spanning the last 800 kyr (Augustin et al., 2004). The accumulation of snow, ice and aerosols and the trapping of air bubbles from previous time periods makes it possible to measure the ratio of stable water isotopes (SWI) and atmospheric concentrations of trace gases including GHG, dust, ash and radioactive substances. From these proxies information of past temperature, precipitation rates, gas concentrations of the atmosphere and events such as volcanic eruptions and forest fires can be extracted. Diffusion and the compressing of the annual layers are important

processes within an ice sheet (Johnsen et al., 2000), causing a reduced time resolution with depth. In this context proxies from many different ice cores are rather well resolved during the Holocene period (last 11,700 years, Steffensen et al., 2008), and variations in the climate can be identified on annual scales.

In the early Holocene a cooling event in the northern hemisphere (NH) 8.2 kyr ago has been identified in many ice cores, e.g. von Grafenstein et al. (1998), Johnsen et al. (2001) and Thomas et al. (2007), and changes in the THC are believed to play a key role in the mechanisms behind this cooling event.

Although ice cores are rich on information, many obstacles has to be overcome when interpreting the different signals in the cores. One problem arises from the fact that SWI signals are only recorded when it snows, making the seasonality of precipitation crucial to the validity of an annual signal. Studies using climate models have been used to estimate any possible bias in the Greenland ice cores.

The purpose of this thesis is to examine

a) if changes in orbital parameters throughout the Holocene causes any bias in the temperature recorded in Greenland ice cores, and to give an estimate of any such bias

b) if the release of freshwater can account for the observed cooling event in the NH 8.2 kyr ago and, in the case of changes in the seasonality of precipitation during the event, to estimate the bias in the same way as in a)

1.1 Outline

In this chapter a description of the various climate models and their evolution will be given, and in Chapter 2 the climate model used in this thesis will be presented in details, from the governing equations to the climate produced by the model. Chapter 3 focuses on the spin-up of the model, necessary to reach a statistical equilibrium state of the climate.

Chapter 4 will be dedicated to experiments, where the model is forced by changes in orbital parameters, simulating Holocene configurations of obliquity, eccentricity and angle between vernal equinox and perihelion. The ability of the model to reproduce high northern latitude climate makes it possible to estimate the changes in the seasonality of precipitation during the Holocene, and when calculating the precipitation weighted temperature, these changes could lead to a bias in the temperature recorded in Greenland ice cores, caused only by changes in seasonality of precipitation. A discussion of the results will be followed by concluding remarks on the topic.

In Chapter 5 experiments are performed simulating the 8.2 kyr event. It is believed that the cooling is caused by sudden freshwater discharges originating from meltwater reservoirs from the Laurentide ice sheet, changing the circulation and heat transport by the world oceans. Results, a discussion and conclusions will be presented.

1.2 Climate models

The ability to predict weather (and thereby the climate) has increased dramatically over the past decades. Although we cannot predict local weather on any given day in the future, computer simulations have made it possible to estimate future climate changes, i.e. the average weather conditions for a given area. The development of climate models can be described by the complexity of the model, from the rather simple Energy Balance Models (EBMs) to fully coupled Atmosphere Ocean General Circulation Models (AOGCMs).

A zero-dimensional EBM treats the entire Earth as a single point, and the system will be in a steady state, when absorbed solar radiation balances outgoing longwave radiation - no energy is accumulated. The absorbed solar radiation is an increasing function of temperature, since the albedo (reflectivity) decreases with increasing temperature[1]. If the outgoing longwave radiation is given by an increasing function of temperature, two equilibrium states for the system may be possible depending on the initial state; one that is totally ice covered, and one that is ice-free (Budyko, 1969 and Sellers, 1969).

When horizontal resolution is allowed, the one-dimensional EBMs include dependence of absorbed solar radiation and surface albedo on latitude, as well as different physical processes such as meridional heat flow. The one-dimensional EBMs break the hemispheres into a number of latitude regions, and the governing equations will depend on the given latitude. This type of one-dimensional EBM was first described by Budyko (1969) and Sellers (1969), and steady state solutions was found for different latitudes of the ice-line.

Using the power of digital computers, local weather prediction models have been developed since the 1950s, and the ability to predict weather has improved with more physical processes, more feedback mechanisms and increased resolution as some of the key progressions in computer modeling. Compared to the simple EBMs described above, these models use non-averaged equations, that are solved numerically in each grid cell and time step defined by the model. Usually a physical grid covers the sphere of the Earth following the latitudes and longitudes, and the atmosphere (and ocean, if represented) is divided into a number of vertical layers.

[1] When temperature increases, the area that is ice-covered decreases, leading to a reduction of the surface albedo.

GCMs use the same set of equations as do weather prediction models, but the objective of a GCM is shifted from short-term weather predictions to long-term trends in the climate of the Earth, with the conservation of energy, moisture and momentum being important conditions in the models. Apart from the dynamical core that integrates the equations, several other sub-grid scale processes have to be taken into account such as convection and cloud processes. This is done by parametrization, whereby the effects of these processes are built into the model by letting the fields, calculated in the dynamical core, be influenced in some way e.g. by the amount of clouds in a certain grid cell.

Today's GCMs include not only the atmosphere and oceans, but also interaction and feedbacks from sea-ice and land-areas, in order to simulate the climate of the Earth more accurately. Fully coupled AOGCMs are the most complex climate models, and studies using different AOGCMs play a large role in climate research and in the prediction of the future climate, e.g. IPCC (2007).

Including more and more components of the climate system, AOGCMs are designed to represent the climate as realistically as possible with one major drawback being the high computational cost. As reported by the IPCC (2007), experiments with AOGCMs are limited to multi-decadal simulations, making it virtually impossible to use this type of computer models to study millennial-scale variations in past and future climate.

The need of comprehensive climate models that are less expensive in computation costs spawned Earth System Models of Intermediate Complexity (EMICs). As in the case of GCMs, EMICs describe most of the atmospheric and ocean processes, but in a more simplified or parametrized form and often with a coarse resolution compared to GCMs. Claussen et al. (2002) proposed a perspective on the hierarchy of climate models, where each model is characterized by the location in a spectrum defined by (i) the number of interacting components of the climate system explicitly described by the model, (ii) order of magnitude of the number of grid cells, and (iii) the sum of spatial dimensions of the atmosphere and ocean components. He found that the gap between EMICs and simple climate models is rather large, whereas the most complex EMICs differ little from most GCMs.

Where GCMs simulate regional climate far more precisely, EMICs have proven to be an effective tool to understanding important processes, and their interactions and feedbacks, within the climate system. Equilibrium states of the climate of various EMICs have been compared to those of a number of GCMs and observations, e.g. Petoukhov et al. (2005), and the general conclusion was, that the scatter in EMIC results is close to that of GCMs, and for both types of climate models, the results agreed well with observations.

As discussed above, the different types of climate models vary in complexity, each with different weaknesses and strengths in simulating the climate.

This should be taken into account, when trying to answer a specific question, and the choice of model (simple or complex) should depend on the question asked.

Chapter 2

The model

In this chapter the model used in this study, ECBilt-CLIO, will be described including the main physics and dynamics. The model consists of an atmosphere (ECBilt) and an ocean (including sea-ice, CLIO) part, that are coupled through fluxes of heat, moisture and momentum. The cycles of these three quantities will be discussed followed by individual descriptions of the two sub-systems, and a short presentation of the climatology of ECBilt-CLIO.

2.1 Heat, moisture and momentum cycles

Solar radiation serves as a heat source for the climate in the model, and short-wave radiation heats the atmosphere and surface respectively. The incoming radiation has a seasonal variation included. From the surface long-wave radiation is emitted and absorbed by the atmosphere, and eventually reemitted into space and back to the surface giving rise to the greenhouse effect. Heat is transported within the atmosphere (oceans) by winds (currents), convection and diffusion. Thermal equilibrium of the system is reached when outgoing long-wave radiation balances incoming solar radiation.

The moisture cycle is primarily driven by precipitation and evaporation. In the atmosphere moisture is transported only in the layers below 500 hPa, and moisture above this height precipitates down to the surface. Precipitation occurs below 500 hPa when the relative humidity exceeds a certain threshold. Evaporation over land is determined by the soil moisture, and sublimation occurs when snow or sea-ice is present. The soil moisture is controlled by precipitation, evaporation, melting of snow over land and run-off. Another threshold for soil moisture determines when run-off from land occurs. River run-off and run-off from land goes into an ocean basin determined by the land-sea mask shown in figure 2.1.

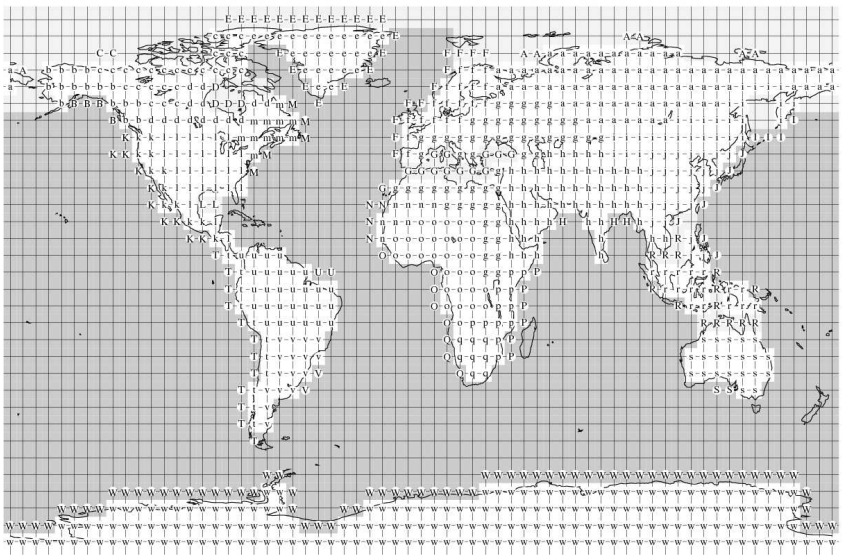

Figure 2.1: *Land-sea mask for ECBilt. Upper case characters indicates run-off area for the region given by the same lower case character. From Opsteegh (1998).*

Diabatic heating produces potential energy which is transferred to kinetic energy. The momentum generated in the atmosphere is subsequently dissipated by internal friction, and transferred to the oceans since surface winds and thermohaline processes drive the currents of the oceans.

2.2 ECBilt

ECBilt was developed by Opsteegh (1998) at *KNMI, De Bilt, The Netherlands* as an alternative to the more complex GCMs developed in the late 1990s, using a dynamical core originally built by Molteni (1993). The goal was to be able to describe the relevant dynamic and thermodynamic feedback processes, but sacrificing resolution in return for faster computation time. In the original paper, model runs of 6 kyr were presented, and decadal-long runs are easily carried out on standard desktop computers nowadays. The following section is based on the work done by Haarsma et al. (1998).

The horizontal resolution of ECBilt is 5.625 $\times$ 5.625 degrees, and the model is spectral with horizontal truncation with wavenumber 21 both zonally and meridionally. The governing equations are discretized on each vertical level, solved in the spectral space and then backtransformed by Fast Fourier Transformation to the physical grid.

Vertically the atmosphere is divided into 3 layers, at 800 hPa, 500 hPa and 200 hPa respectively. The 3 vertical layers are numbered 5,3 and 1

and the intermediate levels 650 hPa and 350 hPa are numbered 4 and 2 respectively. Letting the top of the atmosphere be represented by the 0th layer, in total 6 levels are present in the atmosphere, as well as the surface of the earth, denoted by subscript s.

2.2.1 Dynamics

A fundamental property of the equations of motion used in the model is the quasi-geostrofic approximation, whereby an assumption of geostrophic equilibrium is used in certain contexts of the equations of motion. Parameterizations for the neglected ageostrophic terms are incorporated in the vorticity equation, in order to improve the simulation of the Hadley circulation, e.g. the circulation pattern in the tropics and subtropics, where air masses rise near equator and descend in the subtropics. The flow is poleward in 10-15 km height and equatorward at the surface.

The model is governed by the following quasi-geostrophic equations expressed in isobaric coordinate (i.e. pressure serves as the vertical coordinate):

- The continuity equation:

$$D + \frac{\partial \omega}{\partial p} = 0 \tag{2.1}$$

  where D is the divergence of the horizontal wind, $\omega = \frac{dp}{dt}$ is the vertical velocity and p is the pressure.

- The vorticity equation:

$$\frac{\partial \zeta}{\partial t} + \mathbf{V}_\psi \cdot \nabla(\zeta + f) + f_o D + k_d \nabla^8 \psi = -F_\zeta \tag{2.2}$$

  where $\zeta = \nabla^2 \psi$ is the vertical component of the vorticity vector, $\mathbf{V}_\psi$ is the rotational component, f is the Coriolis parameter (f_o is f at 45°N and S) and ψ is the stream function. k_d is a tunable coefficient for diffusion and F_ζ includes the ageostrofic correction discussed previously.

- The first law of thermodynamics:

  Using the hydrostatic equation

$$T = -\frac{p}{R}\frac{\partial \phi}{\partial p} \tag{2.3}$$

  and the geostrophic relation

$$\phi = f_o \psi \tag{2.4}$$

where T is the temperature, R is the gas constant and ϕ is the geopotential, it is possible to rewrite the first law of thermodynamics in isobaric coordinates as

$$\frac{\partial}{\partial t}\left(\frac{\partial \psi}{\partial p}\right)+\mathbf{V}_{\psi}\cdot\nabla\left(\frac{\partial \psi}{\partial p}\right)+\frac{\sigma}{f_o}\omega+k_d\nabla^8\left(\frac{\partial \psi}{\partial p}\right)+k_R\left(\frac{\partial \psi}{\partial p}\right)=-\frac{RQ}{f_o p c_p}-F_T \tag{2.5}$$

where σ is static stability, k_R is the Rayleigh damping coefficient, c_p is the specific heat capacity, Q is the diabatic heating and F_T is advection of temperature by the ageostrophic wind.

Elimination of ω and D from the equations 2.1, 2.2 and 2.5 leads to one equation for the quasi-geostrofic potential vorticity q:

$$\frac{\partial q}{\partial t}+\mathbf{V}_{\psi}\cdot\nabla q+k_d\nabla^8(q-f)+k_R\frac{\partial}{\partial p}\left(\frac{f_o^2}{\sigma}\frac{\partial \psi}{\partial p}\right)=-\frac{f_o R}{c_p}\frac{\partial}{\partial p}\left(\frac{Q}{\sigma p}\right)-F_\zeta-\frac{\partial}{\partial p}\left(\frac{f_o F_T}{\sigma}\right) \tag{2.6}$$

with q defined by

$$q=\psi+f+f_o^2\frac{\partial}{\partial p}\left(\frac{1}{\sigma}\frac{\partial \psi}{\partial p}\right) \tag{2.7}$$

The two last terms in equation 2.6 result in the ageostrofic forcing, that improves the Hadley circulation by changing the strength and position of the jet stream and eddy activity. In each time step, values for F_ζ and F_T from the previous are used, when solving equation 2.6.

Essentially, equation 2.6 governs the dynamical behavior of the atmosphere. The boundary condition for ω at the top of the atmosphere is given as $\omega = 0$, whereas for the surface of the earth it is given by

$$\omega_s=-\rho_s g(\frac{C_d}{f_o}\zeta_s-\mathbf{V}_{\psi S}\cdot\nabla h) \tag{2.8}$$

where subscript s indicates surface values. From here, equation 2.6 can be applied for each of the three horizontal layers. The temperature balance 2.5 is applied at the two intermediate layers 650 hPa and 350 hPa. The equations for each layer will then include terms that depend on calculations from the layer directly below and above, linking the layers together. The discretized equations can be found in Haarsma et al. (1998).

2.2.2 Planetary boundary layer

Due to the coarse vertical resolution of ECBilt, the planetary boundary layer is not explicitly resolved, and it is necessary to make assumptions about the temperature, moisture and wind profiles in the boundary layer.

Since the temperature is calculated directly for the 650 and 350 hPa layers a relationship for the vertical temperature profile is calculated, using an assumption of a linear temperature profile in the logarithm of pressure

$$T(p)=T_4+\gamma\ln(p/p_4) \tag{2.9}$$

where

$$\gamma = \frac{T_2 - T_4}{p_2 - p_4} \tag{2.10}$$

Numbers as subscripts represent the respective layer. This profile stretches from the surface of the earth to 200 hPa, passing through the computed temperatures at 650 and 350 hPa. Above 200 hPa the temperature is assumed constant.

Combining 2.9, 2.3 and the ideal gas law yields the following expression for the temperature just above the surface

$$T_* = \sqrt{T_3^2 - \frac{2\gamma g}{r}(z_h - z_3)} \tag{2.11}$$

where z_h is the topografic height. It is this extrapolated temperature that is used as the temperature 2 m above the surface.

The relative humidity is assumed constant from the surface to 500 hPa, and the surface wind is assumed to be 80 % of the wind at 800 hPa.

2.2.3 Physics

As described in section 2.1 diabatic heating generates momentum in the atmosphere, and is caused by radiative heating and latent and sensible heat exchange with the surface. The shortwave solar radiation is only reflected at the top of the atmosphere and at the surface, and is reemitted directly into space, neglecting multiple scattering. Absorption of shortwave radiation in the atmosphere (and at the surface) is calculated as a fraction of the incoming radiation, depending on reflection and absorption coefficients, being functions of latitude, time of year and surface type[1]. The longwave radiation scheme is controlled by the vertical temperature profile calculated in equation 2.9, the cloud cover and some empirical constant. The longwave radiation emitted from the surface is given by the Stefan-Boltzmann law σT^4 where σ is the Stefan-Boltzmann constant.

The atmosphere is assumed completely dry above 500 hPa, and the moisture budget below is controlled by the vertical moisture transport, precipitation P and evaporation E. The equation reads:

$$\frac{\partial q_a}{\partial t} = -\nabla_3 \cdot (\mathbf{V}_a q_a) + E - P \tag{2.12}$$

where q_a is the water content in the moist layer of the atmosphere and $\mathbf{V}_a$ is the transport velocity. Since a grid cell is never completely saturated a criterion for rainfall (or snow if $T < 0°\mathrm{C}$) is set up as $q_a > 0.8 q_{max}$ where

[1] Reflection coefficients are essentially the reflection at the top of the atmosphere and the surface albedo.

q_{max} is the vertically integrated saturation specific humidity below 500 hPa. The amount of precipitation is now given by

$$\Delta q_a = \frac{q_a - 0.8 q_{max}}{1 + C} \tag{2.13}$$

where C is a correction for the heating of the atmosphere by condensation of water vapor. The rate of precipitation from a given grid cell, P is given by

$$P = \frac{\Delta q_a}{\Delta t} \tag{2.14}$$

where Δt is one time step.

Evaporation over land and sea, sensible and latent heat fluxes from the surface to the atmosphere and a convective adjustment are parametrized by properties of the surface (land, sea or sea-ice regions) and near surface atmosphere. Different criteria for temperature control soil moisture and snow cover.

This relatively simple hydrological cycle has made it necessary to include a flux-correction, which is described in section 2.4.

The forward integration in time is done using a forth order Runge-Kutta method to solve the quasi-geostrofic potential vorticity equation 2.6, and the time step for the atmosphere is 4 hours.

2.3 CLIO

The Coupled Large-scale Ice Ocean model CLIO results from the coupling of a global, free surface OGCM to a thermodynamical-dynamical sea-ice model. The model has been improved from the first version originally presented by Goosse and Fichefet (1999), and in this study CLIO v. 3.0 is used (hereafter referred to as CLIO). The governing equations were first published in the CLIO Scientific Report by Goosse et al. (2000a).

The ocean part of CLIO includes a relatively sophisticated parametrization of vertical mixing, and is governed by the primitive equations described in details below. The three-level sea-ice component simulates the growth and decay of sea-ice by changes in snow and ice thickness, in response to heat fluxes from the ocean and atmosphere.

The grid cell structure of CLIO is composed of two spherical coordinate systems interconnected at the geographical equator, the southern-most based on classical latitude-longitude coordinates, and the northern subgrid has its poles located at the equator. This is done to avoid a singularity at the North Pole[2]. The rotated subgrid only covers the NA, Arctic and Mediterranean

[2]A singularity at the South Pole does not cause problems since the Antarctic continent covers this area.

Sea, and the connection is done in the equatorial Atlantic where the meridians in one grid corresponds with the parallels in the other. The grid size for both grids is 3 × 3 degrees, and the two grids can be seen in figure 2.2.

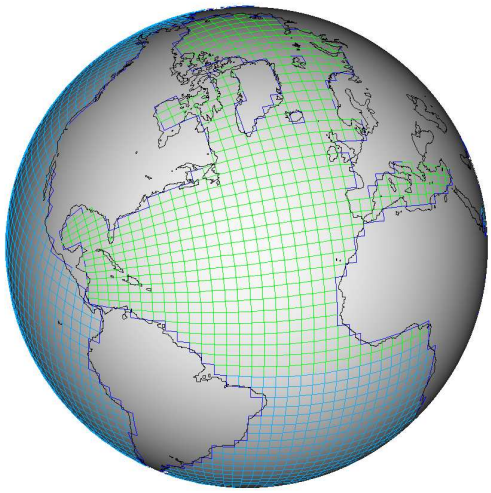

Figure 2.2: *Horizontal grid of CLIO. Classical latitude-longitude grid is shown in blue and rotated grid in green. From Goosse (2000a).*

Vertically the model is composed of 20 layers, where each layer is fixed in depth. The resolution is finest near the surface of the ocean, where strong gradients, vertical mixing and turbulence have a relatively larger influence on ocean properties than deeper down. The top layer is 10 m compared to 750 m in the deepest part of the ocean. The depth of the ocean is determined by the number of active layers in each grid cell, which has been chosen by comparison with real ocean depth, and the depth is therefore represented as steps rather than sloping bathymetry.

2.3.1 Governing equations

The Navier-Stokes equations governs the oceanic flow in the model, here rewritten in a rotating frame of reference, using the following approximations:

- hydrostatic equilibrium is assumed everywhere in the ocean
- the Boussinesq approximation, stating that density differences are negligible compared to the mean density of the ocean, except when they appear in a term multiplied by the gravitational force
- the ocean depth is negligible compared to the radius of the Earth

- horizontal length scales dominates the vertical scales

With these assumptions, the governing equations are

- The continuity equation:

$$\nabla \cdot \mathbf{u} + \frac{\partial w}{\partial z} = 0 \tag{2.15}$$

- The equation of state

$$\rho = \rho(\theta, S, z) \tag{2.16}$$

- The horizontal and vertical momentum equations:

$$\frac{\partial \mathbf{u}}{\partial t} + \mathbf{u} \cdot \nabla \mathbf{u} + w\frac{\partial \mathbf{u}}{\partial z} + f\mathbf{e}_z \times \mathbf{u} = -\frac{1}{\rho_o}\nabla p + \mathbf{F}_{du} \tag{2.17}$$

$$\frac{\partial p}{\partial z} = -\rho g \tag{2.18}$$

- The equations for the time evolution of potential temperature and salinity:

$$\frac{\partial \theta}{\partial t} + \mathbf{u} \cdot \nabla \theta + w\frac{\partial \theta}{\partial z} = F_{d\theta} + F_{v\theta} \tag{2.19}$$

$$\frac{\partial S}{\partial t} + \mathbf{u} \cdot \nabla S + w\frac{\partial S}{\partial z} = F_{dS} \tag{2.20}$$

In this coordinate system x is towards east, y towards north and z upwards. The parameters are as follows: $\mathbf{u}$ and w denotes horizontal velocity in the x- and y-directions and vertical velocity in the z-direction respectively, ρ is density, θ is potential temperature, S is salinity, t is time, p is local pressure, g is the gravitational constant and the Coriolis parameter is $f = 2\Omega \sin\phi$ where ω is the Earth's rotational frequency and ϕ is latitude.

$\mathbf{F}_{du}$ is a correction term for the small scale viscosity processes otherwise not included in the model. The scalar terms $F_{v\theta}$ and F_{dS} accounts for sub-grid processes like isopycnal mixing and eddy induced advection in each grid cell.

2.3.2 Important parameterizations used in CLIO

The vertical mixing in the ocean is parametrized following the work done by Mellor and Yamada (1982), but introducing a background diffusivity region below the surface mixed layer and convective adjustment scheme. The former makes the model perform realistic for regions of low turbulence e.g. the deep ocean, and the latter makes it possible to represent areas of strong convection.

The formation of Antarctic Bottom Water (AABW), the outflow of saline Mediterranean Sea water and several other important processes in the oceans

rely strongly on the process of down sloping currents caused by differences in density. As described earlier in this section the bottom of the ocean is everywhere flat, with step-wise changes in depth from grid cell to grid cell. Down sloping flow is therefore parametrized in a simple way; if dense water spills over a continental shelf, it is moved down to the neighboring (in horizontal direction) grid cell with equal density. The water is assumed to flow along the vertical wall until it reaches a layer with equal density. If it is denser than the entire water column it is moved to the bottom layer.

When decadal-long simulations are needed, it is necessary to have time steps in the order of hours when solving the equations 2.15 through 2.20, which combined with the coarse vertical resolution of the model makes it impossible to represent fast surface gravity waves.

The time step used when integrating the equations for scalars 2.19 and 2.20 is 24 hours, which ensures stability of the system while keeping the computation power needed to a minimum. Exchange between grid cells are performed by fluxes, ensuring that the different conservation laws are fulfilled, and most variables are located in the center of each grid box, following the theory of Messinger and Arakawa (1976).

2.3.3 Sea-ice model

The sea-ice component of CLIO is rather complex including parameterizations of thermodynamic growth and decay and dynamics and transport of the ice. This section will briefly discuss the most important processes, but for a full description the reader is referred to Goosse (2000a).

The growth and decay of sea-ice is basically a function of ice thickness and concentration in each grid cell, meaning that the less ice the faster growth or decay. Vertically the growth and decay of the ice is determined by thermodynamic processes, including heat flux from the ocean and atmosphere to the ice. Horizontal conduction of heat is neglected due to the coarse horizontal resolution, and the one-dimensional heat-diffusion equation used to calculate the evolution of temperature within the ice reads

$$\rho c_p \frac{\partial T}{\partial t} = G(h) k \frac{\partial^2 T}{\partial z^2} \tag{2.21}$$

where h is the ice thickness, k is the thermal conductivity and $G(h)$ is a correction factor for subgrid effects. Equation 2.21 is solved numerically using an implicit method and a time step of 24 hours. The surface temperature of the sea-ice is controlled by an equation of heat balance for the top layer (ice or snow), and at the bottom of the ice slab, and imbalances in the heat budget is corrected for by accretion or ablation of ice.

Imbalances between the heat flux within the ice F_i and from the ocean F_o cause changes in ice thickness calculated by the equation

$$\frac{\partial h}{\partial t} = \frac{F_i - F_o}{L_i} \tag{2.22}$$

where L_i is the heat of fusion of ice.

The horizontal extent of sea-ice is determined by the percentage of the ice-covered area in each grid cell, $1 - A$ where A is the percentage of open ocean in each grid-cell, called the *lead fraction*. Even very small areas of open water in a grid cell can account for important fluxes between the ocean and atmosphere. The lateral growth of ice is parametrized by

$$\left(\frac{\partial A}{\partial t}\right)_{growth} = -\phi(A)\frac{(1-A)}{h_o}C \tag{2.23}$$

where $\phi(A)$ is a decreasing function and $\phi(1) = 0$ and $\phi(0) = 1$. h_o is the ice thickness of the ice created and the constant C is calculated from the heat budget of the ocean surface water, such that ice is created when $C < 0$, and the thickness of the new ice is $h_0/\phi(A)$. When new ice is formed, the ice thickness is averaged with that of pre-existing ice.

A positive heat budget leads to vertical melting of ice, and the thinning of ice eventually causes a reduction in the amount of ice extent[3]. The decay is parametrized by

$$\left(\frac{\partial A}{\partial t}\right)_{decay} = -\frac{A}{2h}\Gamma\left(-\frac{\partial h}{\partial t}\right) \tag{2.24}$$

where Γ is the unit step function. If the ice is thinning $\Gamma(-\frac{\partial h}{\partial t}) > 0$ and hence $(\frac{\partial A}{\partial t})_{decay} < 0$ meaning that when a positive heat budget leads to thinning of ice, lateral decay will also occur.

An equation for conservation of momentum for the 2-D continuum of sea-ice describes the ice dynamics

$$m\frac{\partial \mathbf{u}}{\partial t} = \tau_a + \tau_w - mf\mathbf{e}_z \times \mathbf{u} - mg\nabla\eta + \mathbf{F} \tag{2.25}$$

m being the mass of snow and ice per unit area, τ_a and τ_w are the forces per unit area from the air and water respectively, η is the sea-surface elevation and $\mathbf{F}$ is the internal force per unit area.

If ϑ represents any physical variable that is transported in the sea-ice component, the equation describing horizontal transport used in the model reads

$$\frac{\partial \vartheta}{\partial t} = -\nabla \cdot (\mathbf{u}\vartheta) + D\nabla^2\vartheta + S_\vartheta \tag{2.26}$$

where D is the horizontal diffusivity and S_ϑ is a parametrization of the rate of change of ϑ due to thermodynamic effects. The two first terms on the right-hand side of 2.26 represents advection and diffusion of the physical variable.

The sea-ice component, governed by the equations 2.21 through 2.26, is coupled to CLIO by exchange of momentum, heat and mass at the ice-bottom sea-surface interface, and the time step for the whole sea-ice component is the same as for the ocean part, i.e. 24 hours.

[3]Compared to the vertical thinning, lateral decay of ice is negligible.

2.4 Coupling of ECBilt and CLIO

ECBilt has a fraction of each grid-cell covered by land surface, open ocean or sea-ice. When coupling the two models, these fractions are used to match the area occupied by the three types of surfaces in the two models, in spite of the different grid-cell structure.

Opsteegh et al. (1998) found, that the model overestimated precipitation rates over the Atlantic and Arctic Oceans and a flux-correction was built into the model. A reduction in precipitation of 10 and 50% respectively over these oceans was redistributed over the North Pacific Ocean leading to more a realistic distribution.

Since the atmospheric and ocean time step is 4 and 24 hours respectively, the atmospheric model has 6 time steps for each ocean time step. During these 6 time steps the ocean surface is fixed, and fluxes of heat, moisture and momentum are integrated, and used in the next ocean time step.

2.5 Area and precipitation weights

The output from ECBilt-CLIO is given on the horizontal grid described in section 2.2 and 2.3 respectively. In order to calculate average values over the sphere of the Earth, an area weighted calculation has to be carried out, since the area of each grid cells differs from one another.

The area of a given grid cell can be calculated as

$$A_i = a^2 \cos\phi_i d\phi_i d\lambda \tag{2.27}$$

where i defines the i'th grid cell, A is the area, a is Earth's radius and $d\phi$ and $d\lambda$ is the difference in latitude and longitude respectively. If ϑ_A is any physical variable averaged over the sphere of the Earth, it is calculated as

$$\vartheta_A = \frac{\sum_i \vartheta_i A_i}{\sum_i A_i} = \frac{\sum_i \vartheta_i \cos\phi_i d\phi_i}{\sum_i \cos\phi_i d\phi_i} \tag{2.28}$$

where the summations are for all grid cells. Since a^2 and $d\lambda$ are constants for all grid cells, ϑ_A does not depend on them.

As described in Chapter 1, the precipitation weighted temperature for Greenland during the Holocene, T_{PW} is compared to the regular temperature. The weight is simply calculated by the equation

$$T_{PW} = \frac{\sum_j T_{A,j} P_{A,j}}{\sum_j T_{A,j}} \tag{2.29}$$

where T is the temperature, P is precipitation and subscript A refers to the area weighted calculation of temperature and precipitation respectively given by equation 2.28. The summations over j defines the time interval over which the weight is calculated.

2.6 Climate of ECBilt-CLIO

Opsteegh et al. (1998) evaluated the climate of ECBilt by comparing results from a 500 year experiment with prescribed sea surface temperature (SST, taken from the COARDS dataset) to NCEP-NCAR reanalysis data. The zonally averaged wind and vertical velocity for winter and summer agreed well with observations, whereas the simulation of the stationary planetary waves were too weak. The coupling of ECBilt and CLIO demands that the surface fluxes are realistic, and zonal mean evaporation minus precipitation plots showed good agreement with the NCEP-NCAR dataset, as did the distribution of winter mean precipitation and surface heat flux. The model underestimated the strength of the variability over the NA, and hence the NH storm tracks, but in general, they found reasonably realistic properties of the mean state and variability.

The global ocean circulation of CLIO has been analyzed by Goosse and Fichefet (1999), where they used climatological monthly wind stress, surface air temperature, precipitation and freshwater fluxes, and the humidity of air to force the model. They integrated the model for 1,000 years, and presented results made from averages of the last 10 years of integration. The results discussed here are limited to the NH.

The March and September sea-ice extent and thickness was found to be simulated reasonably well when compared to observations, and deep convection occurred in the Labrador, Greenland, Iceland and Norwegian Seas also in agreement with observations, although the formation of North Atlantic Deep Water (NADW) does not penetrate all the way to the bottom of the ocean north of 40°N as observed (AABW occupies the entire Atlantic ocean).

It should also be noted, that the response in global surface temperature to a doubling of CO_2 is about 1.75 K. This climate sensitivity is in the lower end, when compared to GCMs and other EMICs (Petoukhov, 2005), and it is most likely a consequence of the schematic representation of the tropical atmosphere, given by the ageostrofic correction terms in equation 2.6.

As described in Chapter 3, ECBilt-CLIO has been spun up for 1,500 years before any experiments have been performed. During the spin-up, the model was forced with present-day orbital forcing and pre-industrial GHG concentrations, and after 700-800 years it reached a statistical equilibrium.

Figure 2.3, 2.4, and 2.5 have been produced, taking the average of the last 500 years from the spin-up experiment (see figure 3.1), and the fields presented in figure 2.6 are produced taking the average of a 20 year experiment[4]. These fields are shown to give a general impression of the mean fields produced by ECBilt-CLIO.

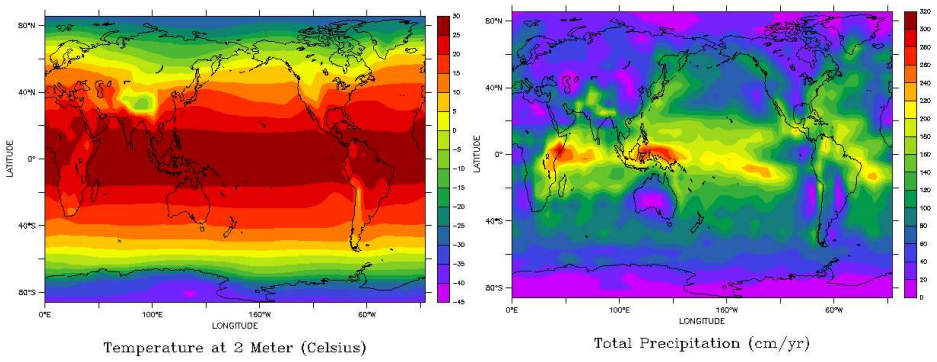

Figure 2.3: *Annual mean temperature at 2 m height (left) and precipitation (right).*

The topography and latitude dependence of the 2 m temperature is clearly visible, but east-west gradients are too weak in the tropics, with too high temperatures in the east Pacific as a consequence (Renssen, 2002).

Xie and Arkin (1997) have used gauge and satellite observations and NCEP–NCAR reanalysis to create a dataset containing global precipitation distributions called CMAP. The distribution in figure 2.3, right shows that areas of high precipitation are located in the tropics across the great oceans, with maxima over south-east Asia and east Africa. The model clearly overestimates the precipitation rates in the latter, but in general the distribution is in good agreement with the CMAP dataset. In the extra-tropics the precipitation is concentrated at the western boundaries of the oceans, and over land it is primarily a function of topography and latitude.

In the left panel in figure 2.4 a clear difference in surface salinity between the Atlantic and Pacific Oceans is seen, especially near the subtropical gyres. The salty outflow from the Mediterranean Sea, rather fresh Arctic Sea near the Bering Strait, and salty surface water off the coast of Chile (caused by low precipitation rates) are other significant features of the surface salinity.

[4]Actually, the salinity and temperature fields of the ocean are produced from the newest version of ECBilt-CLIO called LOVECLIM. This model uses the same atmosphere and ocean/sea-ice components as ECBilt-CLIO, but includes coupled vegetation, carbon cycle and ice-sheet components. The latter three components were deactivated, when experiments with LOVECLIM were performed. LOVECLIM was used, since it was not possible to output the ocean fields from the ECBilt-CLIO version used in the thesis.

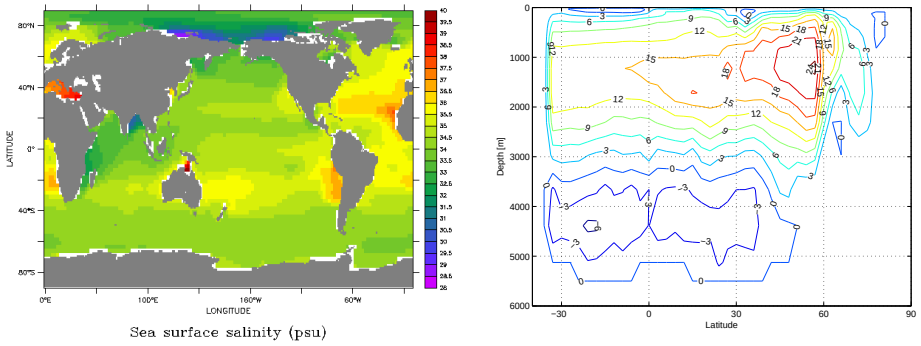

Figure 2.4: *Annual mean sea-surface salinity and latitude-depth distribution of the annual mean MOC in the Atlantic Ocean.*

The circulation in the NA given by the meridional overturning circulation (MOC), figure 2.4 right, shows NADW inflow with a maximum rate of 26 Sv, and 12 Sv being transported to 30°S. The AABW reaches 6 Sv in the deep Atlantic ocean, and is only present below 3,000 m depth. These results are in good agreement with the findings of Renssen et al. (2002).

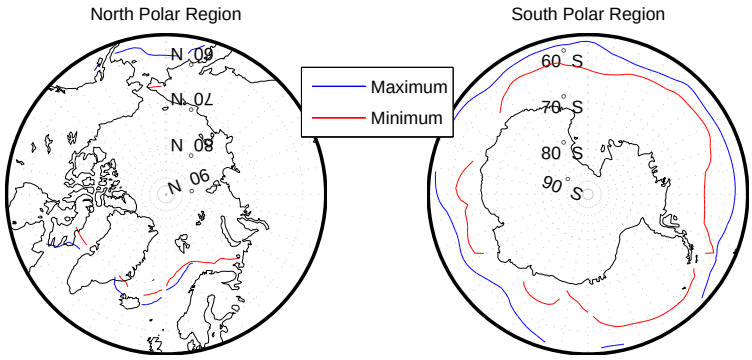

Figure 2.5: *Maximum and minimum sea-ice extent at the poles plotted as 20 cm sea-ice thickness contour levels.*

The maximum and minimum sea-ice extent generated by the model is plotted in figure 2.5, and for both hemispheres it is in fairly good agreement with observations. Maximum (minimum) sea-ice extent is found in March (September).

In figure 2.6 the thermocline can be seen in the top left panel, and the subtropical gyres increase the depth of the thermocline at 30° latitude, and the formation of AABW is seen at high southern latitudes. Along 30°N (top right panel) the temperature distribution at depth is rather stable, with

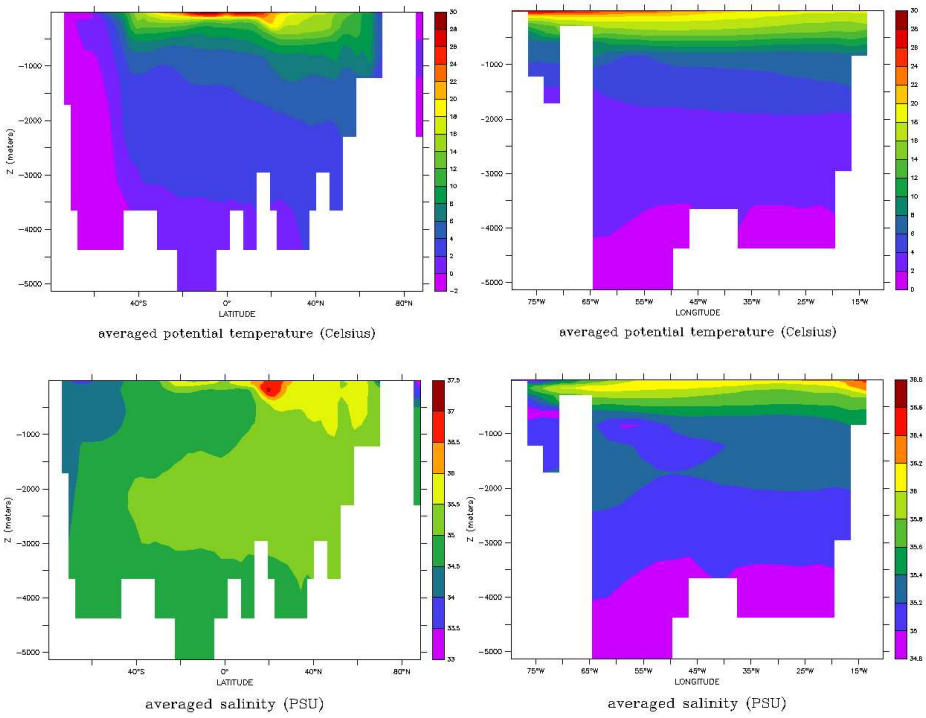

Figure 2.6: *Latitude-depth (at 23° W, left) and longitude-depth at (30° N, right) distribution of the annual mean temperature (top) and salinity (bottom) in the Atlantic Ocean.*

slightly warmer surface temperatures at the western boundary. The depth of the thermocline is 700-800 m across the basin.

The salinity section along 23°W (lower left panel) in the NA shows saline water masses in the subtropical gyres, and the very saline outflow from the Mediterranean Sea. The inflow of rather saline NADW and the fresher AABW can be seen in the deep ocean. The salty subtropical gyres and outflow from the Mediterranean Sea are clearly visible near the surface along 30°N (lower right panel). The western boundary current freshens the surface water by bringing equatorial water masses northward.

2.7 The present study

In the experiments performed in this thesis, focus will be on the high northern latitude atmosphere response to orbital forcing, primarily Greenland (Chapter 4) and the response of ocean circulation and surface temperature in the NA to freshwater discharges in the NA (Chapter 5). In this context,

ECBilt-CLIO has been chosen to perform the experiments for several reasons already described. To summarize,

- ECBilt-CLIO is a coupled atmosphere ocean climate model that is able to reproduce the global climate
- ECBilt-CLIO is particularly good at reproducing the climate of high northern latitudes
- CLIO includes a realistic sea-ice component, that accounts for many important feedback processes
- The low computational cost makes it possible to perform millennial-long experiments

These qualities of ECBilt-CLIO has made it a natural choice for many model studies for past and future climate research. The reader is referred to the *KNMI* homepage[5] for a full list of papers on ECBilt-CLIO.

[5] `http://www.knmi.nl/onderzk/CKO/ecbilt-papers.html`

Chapter 3

Spin-up

Before running model simulations with given forcings, the model has to be spun up. The spin-up time is the time taken for the model to reach a state of statistical equilibrium under the applied forcing, and when modeling Holocene climate the typical forcing used to spin up the model is pre-industrial conditions. When applying different forcings during each experiment, the atmosphere and ocean must then again adapt, meaning that the results should be analyzed after a new statistical equilibrium has been reached, with the new model configuration.

As it is seen below, the spin-up time for the atmosphere part (ECBilt) is much shorter than for the ocean (CLIO), due to the different time scales for atmosphere and ocean circulation. Limited computation power and a large number of different forcing experiments, influences the possibilities in using different spin-up states for each individual experiment.

3.1 Atmosphere spin-up

To look at the spin-up time for the atmosphere, the model was run with prescribed SST and sea-ice climatology instead of the usual CLIO model. It was found, that the annual variability in surface temperature (and all the other physical fields of the atmosphere), was much larger than any initial spin-up, meaning that the spin-up time of the atmosphere is in the order of days to weeks. The horizontal and vertical mixing processes makes it impossible to identify any spin-up of atmospheric fields.

3.2 Ocean spin-up

The spin-up state from which most of the experiments are run uses present day orbital forcing and pre-industrial GHG levels as input to ECBilt-CLIO. In figure 3.1 the global mean surface temperature and maximum MOC in the

NA is shown for both the raw and smoothed data for a spin-up experiment running 1,500 years.

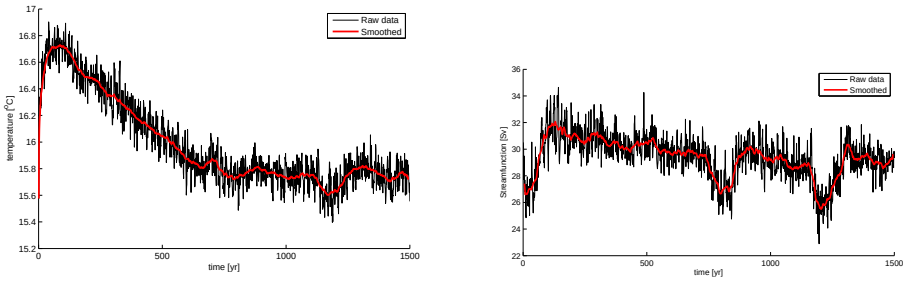

Figure 3.1: *Global mean surface temperature (left) and maximum MOC (right) using present day orbital forcing and pre-industrial GHG levels. Black curve is the raw output and red curve is smoothed using 50 years of running mean.*

After an increase from 15.6 to 16.7°C within the first 30 years follows a relaxation of the temperature towards a constant mean temperature of 15.7°C after 700-800 years. Variations at 700 and 1,200 years indicate, that the variability in surface temperature is around 0.3 K.

Most fields have the same features as the global mean surface temperature. As another example, the maximum MOC increases during the first 100 years from 28 to 32 Sv, and relaxes toward 30 Sv. Excursions are found at the same time-intervals as for the temperature.

After 1,500 years of spin-up, this state is used as a starting-point for the different forcing experiments, described in Chapter 4 and 5.

3.2.1 Overturning timescales

The world ocean can roughly be divided into two regions: a) the upper mixed layer, primarily driven by the wind-stress, large-scale distribution of heat, and fresh water fluxes at the surface of the ocean (typically the top 50-300 meters, depending on latitude, temperature etc.) and b) the deep ocean characterized by the everywhere very cold temperatures (0-4 °C) and the density driven so-called thermohaline circulation. For the former, equilibrium states are reached in a few decades, whereas it can take several hundred years for the deep ocean (Pedlosky, 1996). Since the deep ocean communicates with the atmosphere through the mixed layer, the spin-up time for the climate of a GCM (or, in this case, an EMIC) depends strongly on the timescales of the THC.

Using observations of radioactive tracers in the mixed surface layer and deep ocean, the overturning timescales can be estimated from simple box models, leading to estimates around 1,000 years (Shaffer and Sarmiento,

1995), and similar results ranging from 500 to 1,300 years have been found using OGCMs[1]. Thus, the spin-up time for ECBilt-CLIO of 700-800 years is in good agreement with the general conception of the overturning timescale of the world ocean.

[1]These estimates are based on MOC values simulated by various EMICs and AOGCMs (Gregory et al., 2005).

Chapter 4

Orbital forcing

The study of various isotopes in ice cores from the Greenland ice sheet has revealed detailed climatic records reaching more than 100 kyr back in time. Especially the measurement of SWI such as δO^{18} and δD[1] has been accepted as climatic proxies for many years (e.g. Dansgaard and Johnsen, 1969 and NGRIP members, 2004). These records have shown to be an enormous source of information, helping to understand the natural climate variability during last glacial and the Holocene period. The ability to correctly interpret the δ signals in the cores is of great importance, and in this chapter focus will be on the possible impact changes in seasonality of precipitation can have on ice core interpretations.

The influence of changes in orbital parameters on the meridional temperature gradients (Liu et al., 2003) and on the seasonal changes of oceanic and atmospheric circulation (Masson-Delmotte et al., 1999 and Braconnot et al., 2000) during the Holocene is widely accepted. These changes in circulation patterns can affect the seasonality of precipitation in Greenland, as shown by e.g. Krinner and Werner (2003) and Langen and Vinter (2008). The δ signal in ice cores are precipitation weighted, meaning that a signal is only recorded when it snows, and a change in seasonality of precipitation will thus cause a bias in the signal. If, for instance, the amount of summer precipitation drops, this will appear as a cooling in the signal, even if the temperature is constant.

After a short introduction to the concept of changes in the climate of the Earth due to orbital forcings, the experiments performed with ECBilt-CLIO are described. Results are presented followed by an analysis of the effects this could have on the interpretation of ice cores from Greenland.

[1]The δ notation refers to the ratio of the SWI in a sample compared to that of Standard Mean Ocean Water.

4.1 Milankovitch cycles

The concept of orbital forcing was first described in the 19th century, where scientists promoted the idea that changes in orbital parameters could change the climate of the Earth (Paillard, 2001). In the 1920s Serbian astrophysicist Milutin Milankovitch argued, that the main reason for transitions between glacials and interglacials should be found from the amount of incoming solar radiation reaching the Earth's atmosphere, and that the summer season was critical. Now known as the Milankovitch Theory (Hays et al., 1977), it states that variations in Earth's eccentricity, axial tilt and precession changes the amount and distribution of incoming solar radiation, ultimately affecting the climate of the Earth.

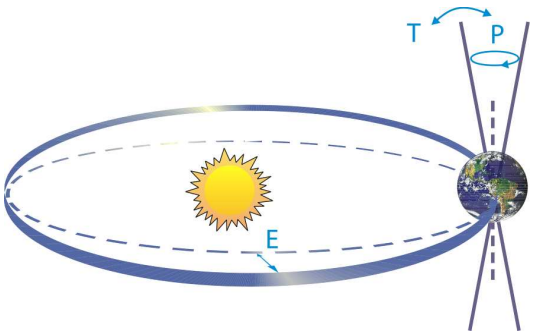

Figure 4.1: *Earth's orbit around the sun with schematic representation of eccentricity E, axial tilt T and precession P. From IPCC (2007).*

Eccentricity is a measure of the shape of the Earth's orbit around the sun, which varies from being nearly circular to mildly elliptical, with different components each with individual periods adding up to two cycles of approximately 100 and 400 kyr. Currently the Earth's eccentricity is low, and the distance to the sun changes little from perihelion (time of year when the Earth is closest to the sun) to aphelion (time of year when the Earth is farthest from the sun), leading to a 6.8% difference in insolation during summer in the two hemispheres. At present perihelion occurs on January 3, and aphelion at July 4, resulting in mild NH seasons and more extreme SH seasons. Throughout the Holocene, eccentricity has been decreasing with less seasonal variations as a result. Eccentricity is the only orbital parameter, that changes the total amount of annual mean solar radiation, which can be seen from figure 4.2 left, comparing the upper and lower panel.

The axial tilt of the Earth with respect to its plane of orbit around the sun, called *obliquity*, varies between 21.5 to 24.5° with a period of 41 kyr. Today obliquity is 23.5° and has been decreasing the last 10 kyr as seen in figure 4.2. If obliquity is small, the insolation is more evenly distributed

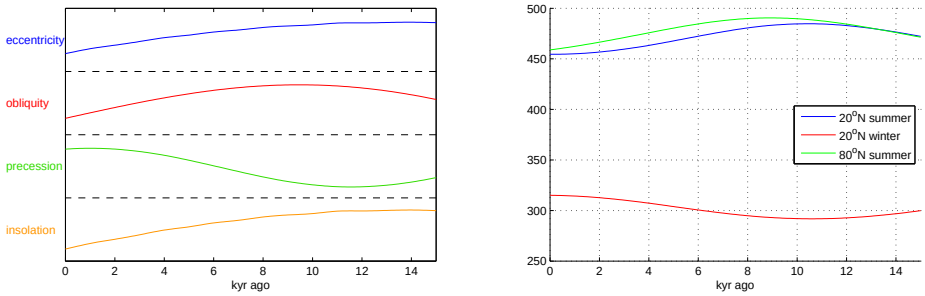

Figure 4.2: *Variations in orbital parameters and annual mean insolation (left) and seasonal mean insolation (right) during the Holocene.*

between summer and winter, making the seasonal variations less pronounced. However, less tilt increases the difference in insolation between the polar and equatorial regions, increasing the meridional gradient of the annual mean solar forcing. The 41 kyr period can be seen in figure 4.3, right panel. Taking a closer look at the top left corner, it can be seen that the high latitudes have received relatively more insolation during the Holocene, and in the future a shift towards a negative deviation from present-day values will occur.

When the Earth rotates around the sun with its axis tilted, it changes the direction of the axis in a wobbling motion with a period of 23 kyr. This *precessional* motion is partly caused by the tidal forces exerted by the sun and the moon, and partly by the precession of the orbital ellipse in space. When winter and summer solstice coincide with perihelion and aphelion respectively, the NH will experience greater seasonal variations since summer occur when the Earth is closest to the sun. As seen in figure 4.2 left panel, the precession was at a minimum at the onset of Holocene, which implies strong seasonal variations. This effect has been decreasing throughout the Holocene, where the summer insolation has dropped $\sim 40\ W/m^2$ for both 20 and 80°N whereas the winter insolation has increased $\sim 30\ W/m^2$ as seen in the right panel.

At high latitudes the annual mean insolation is in phase with obliquity, whereas at low latitudes it is out of phase. The phase shift can be identified at 43° longitude on both hemispheres in figure 4.3, right panel. This phase shift leads to variations in the meridional gradient, and in the left panel the annual mean insolation anomaly calculated for 80°, 50° and 20°N shows a $\sim 5\ W/m^2$ and $\sim 0.5\ W/m^2$ drop and a $\sim 0.9\ W/m^2$ rise in annual mean insolation respectively, since the onset of the Holocene. The effect of this increasing meridional gradient on the climate of the Earth will be discussed in details later.

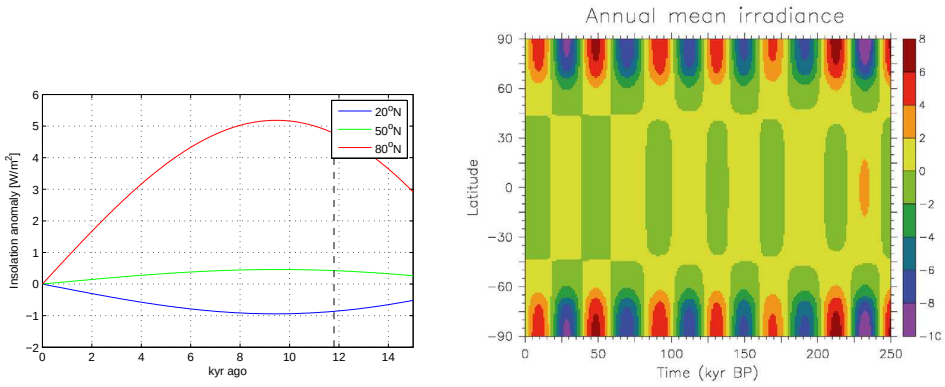

Figure 4.3: *Left: Annual mean insolation anomaly from todays values at 80°, 50° and 20° N. The dotted line represents the onset of the Holocene. Right: Deviation from the present day annual mean insolation over the last 250 kyr. The dominating 41 kyr period and the phase reversal at 43° can be seen very clearly. Right panel is from Loutre et al. (2004).*

To sum up, the changes in orbital parameters during the Holocene has caused

- less seasonal variation (especially in the NH)
- less global annual mean insolation
- an increased meridional gradient of the annual mean solar forcing

Since obliquity, precession and the angle between vernal equinox and perihelion is coupled to each other, knowledge about the former, the latter and eccentricity is enough to calculate the insolation everywhere on the Earth. This is used when calculating the insolation in ECBilt-CLIO.

4.2 Introducing orbital forcing in ECBilt-CLIO

ECBilt-CLIO was originally designed to examine short-term variations in the Earth's climate on the order of a few thousand years, and since the orbital parameters have periods longer than 20 kyr, they were prescribed in the model. It was therefore necessary to incorporate changes in these parameters into ECBilt-CLIO, in order to perform experiments with varying orbital parameters.

The code used to calculate the eccentricity, obliquity and angle between vernal equinox and perihelion is taken from the fully-coupled, global Community Climate Model (CCM) version 3.0[2]. The orbital parameters are

[2]The code was slightly altered to make it compatible with ECBilt-CLIO. See Kiehl et al. (1996) for more details on CCM v. 3.0.

calculated using the formulas described by Berger (1978). For every model run, these parameters change the amount of incoming solar radiation as described in section 4.1, using the start year of the given run as input to the subroutine calculating the three parameters, eccentricity, obliquity and angle between vernal equinox and perihelion.

In the code, the calculation of these parameters are written in a separate subroutine, that is called by the ECBilt component, when the run year is changed forward in time. An on-off switch can be set in the namelist prior to any model run, indicating whether one would use the original values for orbital parameters prescribed by ECBilt or the CCM built-in subroutine.

4.3 The experimental setup

The spin-up state described in Chapter 3 was used as a starting point for the experiments during the Holocene. From here four different snapshot runs were performed 12, 8, 4 and 0 kyr ago, where the incorporated subroutine calculating the orbital parameters for each period forced the model, leading to four different climate states. In figure 4.4 the global mean surface temperature is plotted for the spin-up followed by the four forcing experiments[3].

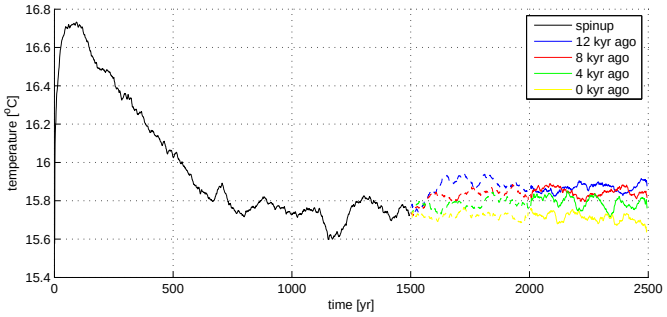

Figure 4.4: *Global mean surface temperature for the spin-up run followed by the four snapshot runs during the Holocene. Data has been smoothed by 30 years of running mean.*

From the spin-up state, the experiments are run an additional 1 kyr, letting the climate adapt to the constant orbital forcing. Within the first 100 years surface temperature responds to the change in solar radiation, with highest temperatures in the early Holocene in good accordance with the decrease in annual mean insolation, seen in the lower panel of figure 4.2.

The results presented in the following section compares fields of physical parameters for the four experiments, with temporal and spatial resolution

[3]The endpoints has been left out of the figure, since the smoothing led to large fluctuations.

given by ECBilt-CLIO. However the results presented are calculated averaging over the last 500 years of each experiment, shown as solid colored curves in figure 4.4, smoothing out any natural decadal variability that may occur.

4.4 Results

The results in this section primarily focus on temperature and precipitation, leading to calculations of precipitation weighted temperature in Greenland for the experiments. Other fields of interest are presented in section 4.4.3.

4.4.1 Temperature and precipitation

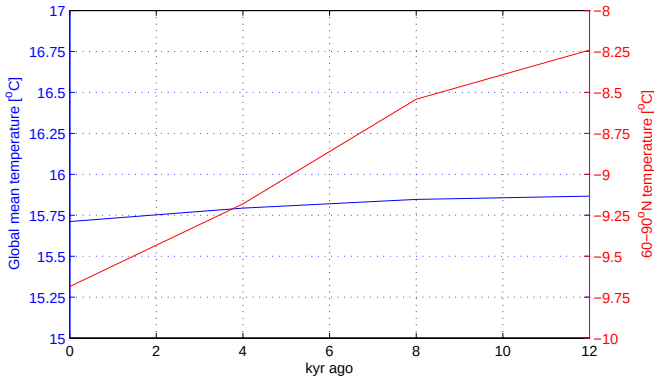

Figure 4.5: *Global and 60-90°N mean surface temperature during the Holocene.*

The global and 60-90°N mean surface temperature is calculated for each experiment and plotted in figure 4.5 against time. The global temperature decreases 0.16 K whereas the entire north polar region responds much stronger with a decrease of 1.5 K during the Holocene. The linear decrease in global mean temperature during the Holocene is a response to the decreasing amount of total insolation seen in figure 4.2 bottom panel.

Since the 80°N summer insolation peaks 9 kyr ago and decreases fastest between 6 to 2 kyr ago, this can explain the relatively larger change in 60-90°N mean temperatures in the mid Holocene.

Langen (2005) has investigated the mechanisms of polar amplification using the CCM. Forcing the model with perturbations in surface temperature in the tropics, extra-tropics and over the entire Earth, a so-called ghost forcing, he found a typical polar amplification pattern as a response to the forcings applied. The polar amplification was found to be a superposition of a global response to a tropical forcing and a local response to a high-latitude

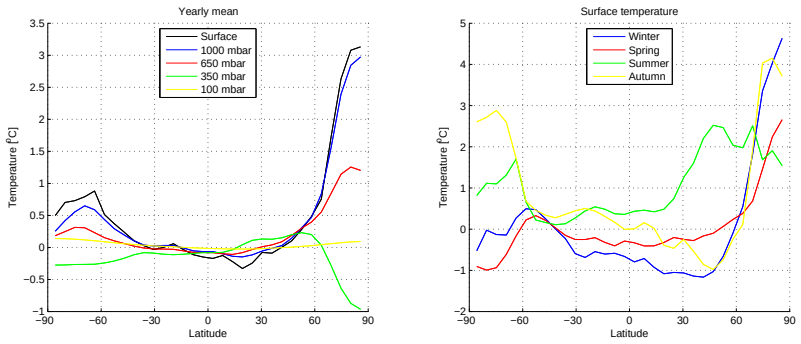

Figure 4.6: *Left: Zonal mean temperature for the surface and the four layers in the vertical, plotted as the difference between 12 and 0 kyr ago. Right: Zonal mean surface temperature averaged over each season, again plotted as the difference between 12 and 0 kyr ago.*

forcing. Furthermore tropical SST perturbations led to warmer and more moist conditions in the high-latitude troposphere. The explanation could be found from the fact, that the poleward heat transport increases both with an increasing meridional temperature gradient as well as an increase in global mean temperature.

Where Langen used a simplified setup without albedo feedback and sea-ice, the ECBilt-CLIO results presented here all include the dynamic sea-ice component described in Chapter 2, as well as changes in surface albedo. The orbital forcing leads to somewhat similar polar amplification patterns seen in figure 4.6. It is clear that the NH shows a much larger amplification than the southern, caused by differences in land, ocean and sea-ice distribution and circulation patterns.

Another important feature is the decreasing polar amplification with height, seen in the left panel. The 350 hPa temperature shows a warming trend during the Holocene. Cai (2006) used a simple 4-box model to show that changes in the radiative forcing, can lead to a positive polar amplification on the surface, whereas the atmosphere can exhibit a negative polar amplification. This can explain the negative trend in the 350 hPa curve.

In the right panel, the polar amplification is shown for each season. Where the south polar region only shows polar amplification during boreal summer and autumn, all four seasons show polar amplification at high northern latitudes. Winter and autumn temperatures decrease up to 4 K, and 2 K during spring and summer.

The negative values in winter, spring and autumn temperatures from 30°S to 50°N might be the result of a 2-4% increase in the Atlantic heat transport from 12 kyr ago to today in this region (not shown).

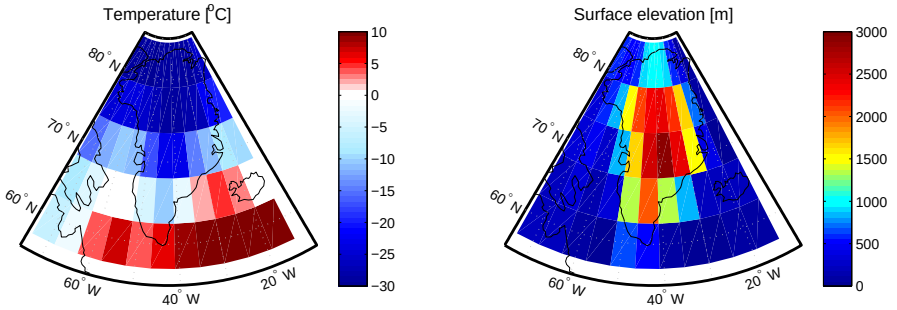

Figure 4.7: *Present day surface temperature (left) and surface elevation (right) for Greenland.*

Using present day conditions, the spatial variations in temperature in Greenland is given in figure 4.7 together with the topography. Obviously a meridional gradient accounts for large differences in temperature in Greenland, but it is also strongly influenced by the topography. The annual mean temperature of the southern tip of Greenland is very high; -9° compared to -15° given by assimilated ERA40 data, whereas central Greenland shows more realistic temperatures around -20 to -35°C (see section 4.5.1). Except for the northern most region of Greenland, it is clear that the coastal temperatures are dependent on the topography, with decreasing temperatures as a function of height.

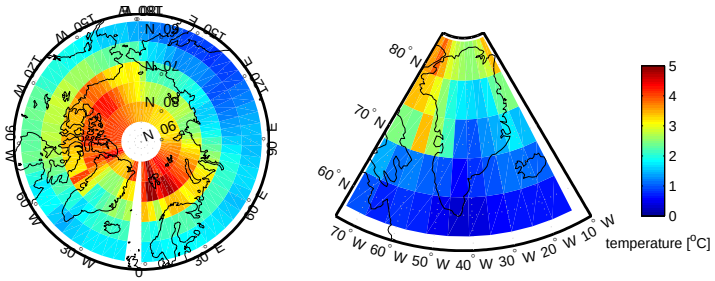

Figure 4.8: *Surface temperature change during the Holocene, plotted as the difference between 12 and 0 kyr ago temperatures. The singularities at the North Pole and along the 2.25° W longitude are due to the grid cell structure used in ECBilt-CLIO.*

The spatial difference in annual mean temperature in Greenland during the Holocene is plotted in figure 4.8 as the difference between 12 and 0 kyr ago temperatures. The increased polar response is clearly visible in the left

panel, with the Barents Sea showing changes up to 5 K, and in general land areas show smaller temperature change than sea areas. In Greenland the temperature change decreases with latitude from 2.5 K in the north to 0.5 K in the south, and in the center of the ice cap the change is around 1.5-2.0 K.

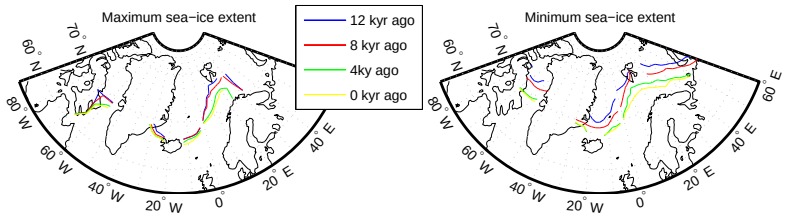

Figure 4.9: *Sea-ice extend in March (left) and September (right) for the four experiments. The contour-lines are plotted for 20 cm sea-ice thickness.*

The cooling of the Barents Sea can be explained partly by changes in the sea-ice extent. As seen in figure 4.9 the sea-ice extent has increased during the Holocene, and the advance of minimum sea-ice extent is most notable in the right panel, comparing the blue and yellow curves. Grid cells that are sea-ice covered, can allow the surface temperature to cool further than grid cells with open ocean, since sea-ice acts as an insulator from the ocean SST as described in Chapter 2, thereby increasing the negative temperature change from 12 kyr ago to today.

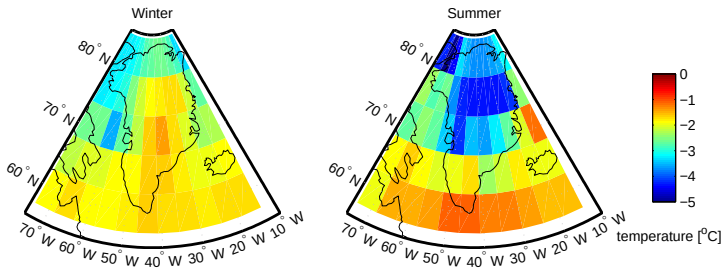

Figure 4.10: *Winter (left) and summer (right) surface temperature change during the Holocene, plotted as the difference between the temperatures 12 kyr ago and today.*

Figure 4.10 shows the seasonal temperature change in Greenland, and most notable is the 4 K decrease in summer temperatures in central and

northern Greenland, compared to a 1.5 K decrease in winter temperatures. Since the winter insolation is constant (zero) for high latitudes throughout the Holocene, the summer change is expected to be larger than the winter. The mechanisms of polar amplification discussed earlier (global response to tropical forcings), and the fact that the sea-ice extent and ocean temperatures are influenced by the decreasing summer temperature, can explain the decrease in winter temperature.

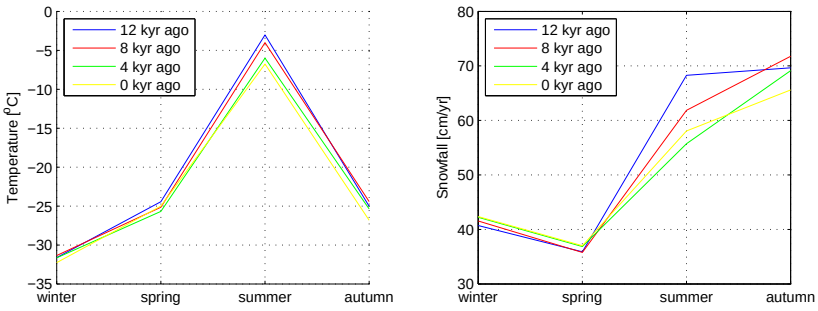

Figure 4.11: *Seasonal temperature (left) and snowfall (right) averaged over Greenland during the Holocene.*

For each of the experiments performed during the Holocene, the changes in the seasonal temperature and precipitation signals in Greenland can be seen in figure 4.11, and for each season the fields are calculated as the mean of the climatology of the three months in each season. The spatial average is calculated for all the land grid cells covering Greenland, given by the land-sea mask in figure 2.1.

Where both the winter and spring temperature and snowfall changes little during the Holocene, the increased summer response can be identified in both the left and right panel. In the autumn, the temperature change is slightly more pronounced than in spring. The autumn snowfall change is almost as large as during summer.

The summer temperature decreases chronologically 4 K, but shifts in the autumn with higher temperature 8 kyr than 12 kyr ago. This can be explained by changes in orbital parameters discussed in section 4.1, and from figure 4.2 it is seen that the 80°N summer insolation peaks around 8.5 kyr ago, whereas the global annual mean insolation decreases throughout the Holocene, bottom panel in figure 4.2.

The seasonal cycle in snowfall shows relatively small amounts of winter and spring snowfall ($\sim$ 40 cm/yr) compared to summer and autumn (55-70 cm/yr). The summer snowfall drops from 68 cm/yr 12 kyr ago to 57 cm/yr 4 kyr ago, and in the autumn the snowfall peaks at 72 cm/yr 8 kyr ago to

present day values at 65 cm/yr[4].

	12 kyr ago	8 kyr ago	4 kyr ago	0 kyr ago
ratio summer/total	0.318	0.293	0.273	0.286
annual avr. [cm/yr]	53.6	52.7	51.0	50.8

Table 4.1: *Ratios of summer to total and annual averaged precipitation in Greenland during the Holocene.*

Seasonal changes in the snowfall can also be seen from the ratio of summer relative to total snowfall shown in table 4.1. A decrease during most of the Holocene, from 31.8% 12 kyr ago to 27.3% 4 kyr ago, results in relatively larger summer weighting in the early Holocene, although the ratio increases slightly over the last 4 kyr. The annual mean snowfall decreases 2.8 cm/yr as a result of the changes in the orbital forcing.

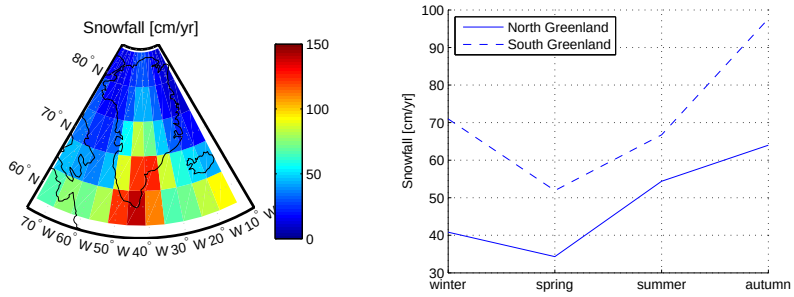

Figure 4.12: *Left: Present day annual mean snowfall in Greenland. Right: Changes in seasonal snowfall for north and south Greenland.*

Looking at the spatial distribution of snowfall in Greenland in figure 4.12, it is clear, that south Greenland receives more snow than the north, which is in agreement with observations (see section 4.5.1). Dividing Greenland at 74°N in a northern and southern part, it can be seen from the right panel, that south Greenland receives an equal amount of winter and summer snowfall (70 cm/yr), and almost 1 m/yr in the autumn. In north Greenland the amount of snowfall is smaller, but since it covers a larger area than south Greenland[5], this has greater influence on the total snowfall in Greenland.

[4]Limitations in computer storage made it impossible to output monthly mean for the full 500 year runs used in the experiments, but shorter runs showed, that the autumn snowfall was dominated by large September snowfall compared to October and November. This could suggest, that the large autumn snowfall is biased towards summer snowfall.

[5]With the grid cell structure of ECBilt-CLIO, the area of north and south Greenland is 40.8 and 15.5×10^6 km^2 respectively.

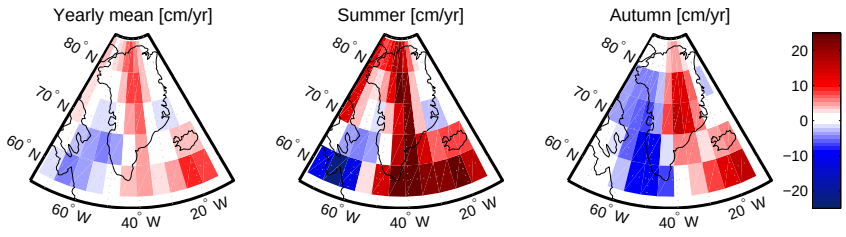

Figure 4.13: *Yearly mean, summer and autumn snowfall plotted as the difference between the snowfall 12 kyr ago and today.*

The change in seasonal snowfall is plotted as the difference between 12 kyr ago and today, for annual mean, summer and autumn rates in figure 4.13. Winter and spring are left out, since these seasons show very little changes as discussed earlier. Positive values represent larger snowfall 12 kyr ago than today and vice versa.

Common to all three panels is the large change in snowfall in central Greenland, whereas the coastal regions show less variation. The change in snowfall is largest during summer between 30 and 40°W (up to 25 cm/yr), and the change is most pronounced in four grid-cells in central and east Greenland during autumn ($\sim$ 15 cm/yr). This easterly shift could be caused by changes in the atmospheric circulation (see section 4.4.3).

4.4.2 Precipitation weighted temperature

From the results presented previously, it is now possible to calculate the precipitation weighted temperature for the four experiments, as described in Chapter 2. The changes in seasonality of the snowfall in Greenland during the Holocene cause a larger weight of the summer and autumn temperatures in the early Holocene compared to the regular temperature[6].

In figure 4.14 the annual mean temperature for Greenland compared to the precipitation weighted temperature for the different orbital forcings are shown together with the difference between the two. The regular and precipitation weighted temperature drops 1.8 $\pm$ 0.1 and 2.5 $\pm$ 0.5 K, respectively, throughout the Holocene. The difference, plotted in red, shows a shift in precipitation weight around 4 kyr ago: from 12 to 4 kyr ago, the effect of the weight has been decreasing fairly linear from 1.6 $\pm$ 0.4 to 0.7 $\pm$ 0.4 K, and in the last 4 kyr this effect has been almost constant. The precipitation weighted temperature is higher than the regular due to the fact that more snow falls during summer and autumn. The 0.9 $\pm$ 0.4 K shift in precipitation weight will be discussed in details later.

[6]The term 'regular' temperature refers to the temperature calculated directly be the model.

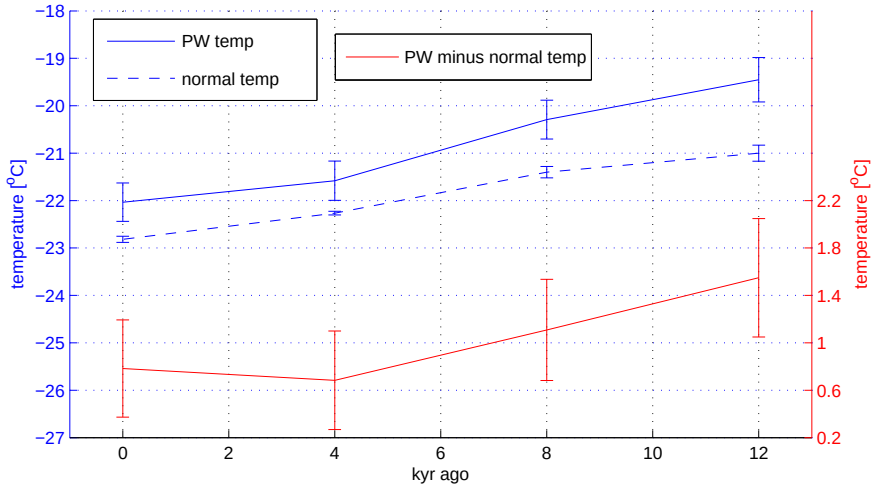

Figure 4.14: *Annual mean precipitation weighted and regular temperature in blue, and the difference between the two in red. Error bars represent two standard deviations.*

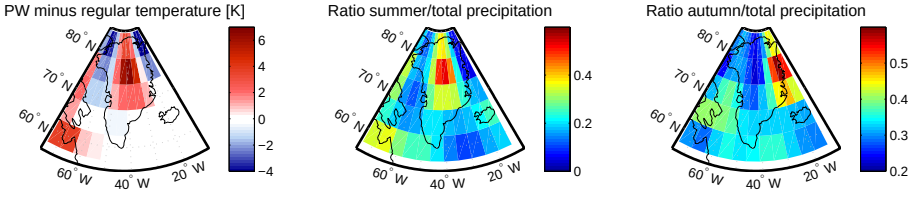

Figure 4.15: *Difference between regular and precipitation weighted temperature for Greenland and the ratio of summer and autumn to total precipitation for the present day experiment. Note the different scales.*

For the present day experiment, the precipitation weighted minus the regular temperature is shown in the left panel in figure 4.15, and the ratio of summer (autumn) to total precipitation in the center (right).[7] The weighted temperature shows the largest change in central Greenland, with up to 7 K difference from the regular temperature, and in north Greenland the difference is also clearly visible. In the coastal regions and south Greenland the value is close to zero and some places even slightly negative. Comparing with figure 4.13 it can be seen, that the grid cells showing the largest difference are also the areas with the highest increase in summer and autumn precipitation during the Holocene.

[7]Only the present day experiment is shown, since these type of plots are very similar for all four experiments.

From table 4.1 the summer to total precipitation ratios were calculated as an average over Greenland. Looking at the spatial resolution in Greenland, the middle panel in figure 4.15 shows great resemblance with the left panel, indicating that the summer precipitation has the greatest influence on the weighted temperature, even with higher precipitation rates during autumn (see figure 4.11). Changes in the autumn to total ratios are primarily seen on the west coast. In central Greenland the summer to total ratio is 0.5, meaning that half of all the precipitation occurs during summer, indicating that the temperature recorded in ice cores from central Greenland has been warm biased, even more than the 1 K shift, shown in figure 4.14 for the whole Greenland ice cap.

4.4.3 Atmospheric Circulation

Changes in atmospheric circulation are important since these circulation patterns determine the amount of snowfall and source regions for Greenland precipitation. Most easily visualized is the seasonal mean geopotential height, indicating the strength and direction of the geostrofic winds.

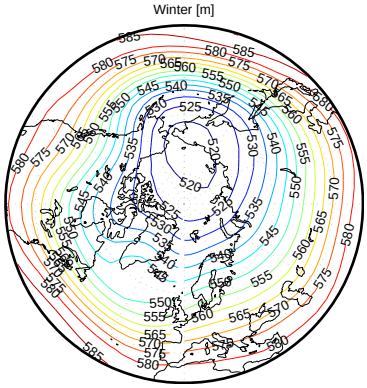

Figure 4.16: *Winter mean geopotential height of the 500 hPa layer for the present day experiment.*

Figure 4.16 shows that the source regions for northern Greenland precipitation could be found in the north Pacific, however the circulation direction changes very little in the four experiments (not shown), indicating the the Greenland moisture sources are much alike throughout the Holocene.

From figure 4.11 it is seen, that the amount of snowfall changes the most in summer and autumn, indicating that the largest variations in atmospheric circulation should be found in these seasons as well. In figure 4.17 the difference in geopotential height between 12 kyr ago and today is plotted for

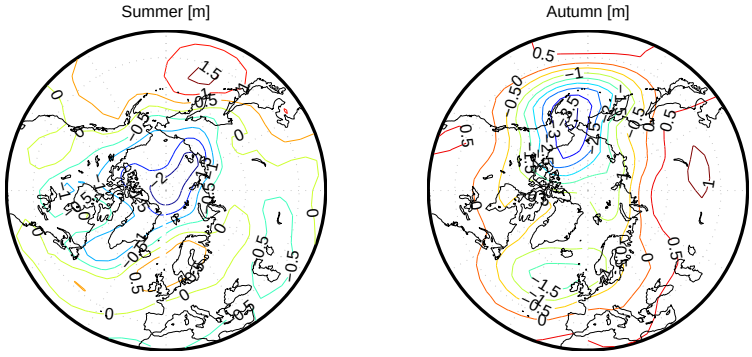

Figure 4.17: *Summer and autumn mean geopotential height of the 850 hPa layer, plotted as the difference between the geopotential height 12 kyr ago and today.*

the 850 hPa layer for these seasons, and they both show an increase in the geopotential height across the Arctic Sea during the Holocene, leading to an increase in the strength of the circulation in the polar cell. This can also be seen in the 850 hPa wind field (not shown) which increases in strength during the Holocene at high latitudes.

4.5 Discussion

The discussion is split into two parts: a comparison with proxy data and a presentation of other model studies on the topic of Holocene climate variability. The former discusses the validity of the model results, when compared to ice and sediment cores and the ERA40 reanalysis dataset, and the latter will focus on studies using a broad spectrum of EMICs and GCMs.

4.5.1 Comparison with proxy data

The temperature change in Greenland during the Holocene has been estimated from ice core studies. Johnsen et al. (2001) estimated a cooling of 3 K for the NGRIP record since the climatic optimum 8.6 kyr ago. Similar, but less pronounced, results were obtained for the GRIP record, indicating that the Holocene cooling was more intense in north Greenland. From sediment cores across the NA and Polar Seas, a cooling between 1.5 and 4 K has been reported (i.e. Andersen et al., 2004, Marchal et al., 2002, and Rimbu et al., 2003).

Comparing the results from the present study, the temperature drop in Greenland is 1.8 $\pm$ 0.1 K during the Holocene. However, this change in

temperature is for experiments 12 kyr ago compared to present day, and the cooling from 8 kyr ago is only 1.4 K (figure 4.14). Although the decrease in temperature is low compared to the data, the shift in precipitation weighted temperature around 4 kyr can explain the difference; the precipitation weighted temperature change in Greenland is 2.5 ± 0.4 and 1.7 ± 0.4 K the last 12 and 8 kyr respectively, closer to what is found in the ice cores.

An increased response in north Greenland temperature change was also found, in agreement with the difference between NGRIP and GRIP, and the 60-90°N average temperature showed a cooling of 1.5 K, which is in the lower end of the estimates from sediment cores.

In table 4.1 the annual mean precipitation rates in Greenland for the four experiments are around 50 cm/yr. From ice core studies Johnsen et al. (1992) and NGRIP members (2004) have found 'observed' present day precipitation rates in Greenland ranging from 17 cm/yr in central and north Greenland to 51 cm/yr in the south, suggesting that the model overestimates the amount of snowfall. This may be caused by a too large influence of the Atlantic storm track, and the fact that the step-wise changes in surface elevation from grid cell to grid cell leads to high precipitation rates. In general, precipitation is not easily modeled. The relatively simple hydrological cycle and coarse resolution of ECBilt-CLIO are reasons for the discrepancies between observed and modeled precipitation.

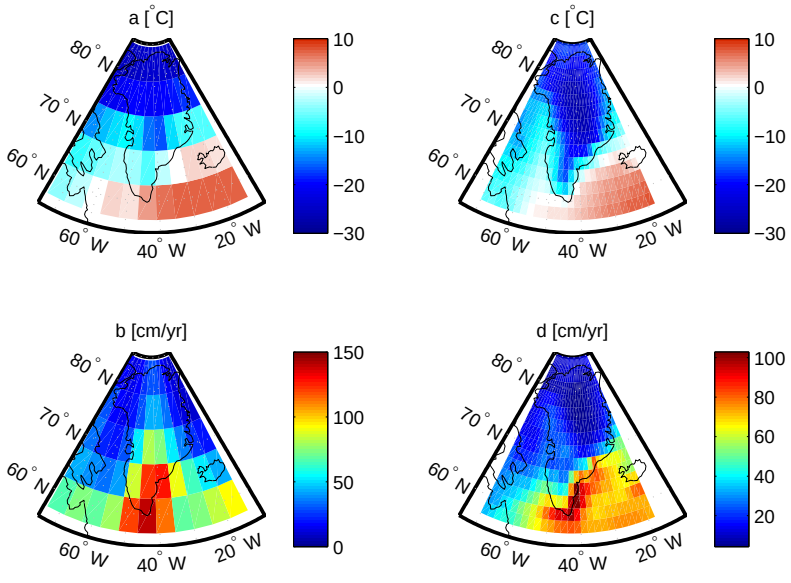

Figure 4.18: *Annual mean surface temperature (a, c) and precipitation (b, d) in Greenland from ECBilt-CLIO (a, b) and from the ERA40 dataset (c, d). Note the different scalings for precipitation.*

The temperature and precipitation rates in Greenland for the present day experiment have been compared to assimilated ERA40[8] data in figure 4.18. Discrepancies in temperature between ECBilt-CLIO and ERA40 data include coastal region variations, and south Greenland temperature, but in central and north Greenland the temperature is in good agreement. The general distribution of precipitation on the Greenland ice sheet is in good agreement with the data, with most snowfall close to the south-eastern tip of Greenland, but the model clearly overestimates the rates, especially in central and south Greenland.

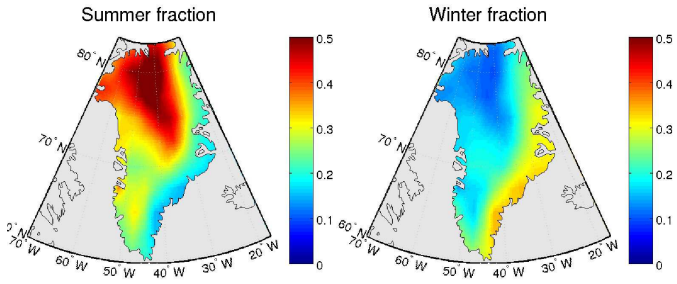

Figure 4.19: *Ratio of summer and winter to total precipitation from the ERA40 dataset.*

The summer fraction of precipitation from the ERA40 dataset shown in figure 4.19 is more detailed than that produced by ECBilt-CLIO (figure 4.15). Where the ratio in central Greenland is 0.5 in the model, a 'tongue' stretches from north-west to central Greenland in the assimilated data, with a maximum ratio of 0.5. As was the case for temperature, the model fails to reproduce any significant signal along the coasts of Greenland, and the coarse resolution of ECBilt-CLIO might be a possible explanation for the differences between the assimilated data and modeled ratios.

It should be noted that the state of the climate from which the experiments are performed does not take into account the transition of the major ice sheets from last glacial period to the Holocene climate (see Chapter 3). Where the temperature recorded in the ice cores increased during the transition and peaked at the climatic optimum 8.6 kyr ago, no such variations are simulated in the experiments, where the variations in temperature and precipitation responded only to changes in orbital parameters 0, 4, 8 and 12 kyr ago. However, the differences in various fields between the 12 kyr ago and present day experiments still capture the main mechanisms for changes in precipitation weighted temperature, leading to a possible warm bias in the temperature recorded in the ice cores as argued above, regardless of the missing simulation of the temperature increase during the transition from

[8]Data obtained from http://www.ecmwf.int/research/era/do/get/era-40

glacial to Holocene climate.

4.5.2 Other model studies

AOGCM studies by Liu et al. (2003) showed a cooling of the Arctic region of ~ 1 K since the early Holocene as a response to changes in orbital forcing. Renssen et al. (2005) have used a version of ECBilt-CLIO that has a dynamic global vegetation model coupled to the atmosphere and ocean part, ECBilt-CLIO-VECODE, to study the high northern latitude climate during the Holocene. A transient simulation over the Holocene, where the model was forced with changes in orbital parameters and GHG concentrations (CO_2 and CH_4) showed a decrease in annual mean temperatures of 1-3 K, a reduction in summer precipitation and an expansion of the sea-ice extent, very similar to the results presented in this study, although they found that the GHG forcing partly counteracted the decrease in summer insolation. Of special interest is their results for the Greenland ice sheet, showing a clear change in seasonality of precipitation in central Greenland, with the fraction of summer to total precipitation decreasing 10% during the Holocene. Where the summer fraction in the experiments described in section 4.4 only show a 3% decrease for the Greenland mean, figure 4.15 indicates that this value is substantially higher in central Greenland, consistent with the result of Renssen et al. (2005).

The decrease in summer temperature cause an expansion in the minimum sea-ice extent, with an increase in surface albedo and a decrease in heat transport from the ocean to the atmosphere as a consequence, and these two positive feedback mechanisms enhance the temperature response at high latitudes. Renssen et al. (2005) analyzed the effects of the expansion in the sea-ice extent and found that, besides the ice-albedo and ice-insulator feedbacks, a strong influence of changes in sea-ice extent on the precipitation near the ice-line. It is very possible that the same mechanisms influence the changes in precipitation in Greenland presented previously, given the close relationship between the models used to perform the experiments.

Many studies of the impact of changes in seasonality on the interpretation of the signals recorded in ice cores have been published, e.g. Werner et al. (2000), Krinner et al. (1997, 2003), Masson et al. (2000), Johnsen et al. (2001) and Langen and Vinter (2008), and it is widely accepted that such changes can account for some of the discrepancy between the temperature calculated from 'classical' δO^{18} records and that from borehole and gas diffusion thermometry (Krinner, 2003 and references therein). Where the former indicates a 10 K difference in temperature between present day and Last Glacial Maximum (LGM), the latter has shown that LGM surface temperatures were about 20 K colder than today. In this study, a warm bias of 1 K for the entire Greenland ice sheet is found during the Holocene, with the possibility of even higher biases in central Greenland.

Changes in moisture source regions for both Greenland and Antarctic precipitation have been reported during the Holocene, as a possible explanation for fluctuations in the deuterium excess[9] records from different ice cores, e.g. Masson-Delmotte et al. (2005a) and Vimeux et al. (2001). Where δO^{18} and δD are used as high-latitude temperature proxies, the deuterium excess can be used to obtain information on remote changes, e.g. changes in moisture sources. Both studies attribute some of the changes in the deuterium excess to a stronger atmospheric circulation throughout the Holocene, with a possible influence on the seasonality of precipitation in the Antarctic and Greenland ice sheets. This is consistent with the model results presented in section 4.4.3, where the circulation in the polar cell has been increasing since the early Holocene.

Turning to the LGM, Langen and Vinter (2008) used the CCM to track the changes in moisture sources for Greenland precipitation to glacial boundary conditions, and found that at the LGM the moisture sources were shifted toward the Pacific, thereby altering the signal in the Greenland ice cores. Moreover, they found that in the annual mean, the changes could be decomposed into linear contributions from temperature changes, seasonality changes and source distribution changes. This supports the idea that the cooling recorded in Greenland ice cores throughout the Holocene is a combination of a decrease in temperature and warm bias in the early to mid Holocene caused by a shift in the seasonality of precipitation.

Loutre et al. (2004) have examined the effect of changes in orbital parameters on climate. Where classical Milankovitch theory focuses on the high latitude NH summer insolation, as the main forcing controlling glacial-interglacial variations, they show that changes in obliquity are more likely to be responsible for the climate variations seen in some paleoclimate data. Moreover, they found that the meridional gradient of annual mean solar forcing has large impact on climate variations. For instance, an increase in the meridional temperature gradient, could account for a greater poleward moisture transport, thereby affecting the seasonality of high-latitude precipitation, in a similar way as found by Langen and Vinter (2008) and in this study.

The results presented in section 4.4 show a somewhat similar pattern. The meridional temperature gradient increases leading to a polar amplification. This affects the atmospheric circulation and thus the moisture transport to and the amount of precipitation in the polar regions. The summer and autumn precipitation ratios seems to be affected the most by these changes.

[9]The deuterium excess d is defined by Dansgaard (1964) as $d = \delta D - 8\delta O^{18}$.

4.6 Conclusion

Experiments have been performed with the intermediate complexity atmosphere - ocean - sea-ice model ECBilt-CLIO, simulating the climate at various periods during the Holocene. After an initial spin-up time, the model was forced by changes in orbital parameters calculated 12, 8, 4 and 0 kyr ago by an incorporated subroutine in the model code. These four experiments led to different states of the climate, and focus has been on high northern latitudes, particularly Greenland, a region in which the modeled climate has proven to be in good accordance with the observed climate.

Both proxy data and other model studies have shown a decrease in surface temperature in the NA region and in Greenland. Model results showed a 0.16 K decrease in global mean temperature during the last 12 kyr, whereas the 60-90°N and Greenland mean temperature decreased substantially more; 1.5 and 1.7 K respectively, which is in the lower end of what has been found in proxy data and with other models.

This polar amplification is most pronounced close to the surface and in winter and autumn, probably due to variations in the ice extent, with various positive feedback processes, such as the ice-albedo and ice-insulator feedbacks, playing important roles in the temperature response at high northern latitudes.

The temperature change in Greenland occurs mostly during the summer season, which matches the seasonal variation in high latitude solar insolation; the insolation is zero during the winter and most of spring and autumn, and hence variations in the summer insolation are most important for the heat budget. The temperature change is largest in north and central Greenland (up to 4 K). These results are consistent with what has been found in other model studies. As was the case with temperature, the changes in precipitation rates in Greenland are highest in central Greenland in the summer, and to some extent in autumn, in good agreement with the changes in circulation patterns. The ratio of summer to total precipitation is 3% lower in the present day experiment than 12 kyr ago, and some areas in central Greenland the summer precipitation accounts for 50% of the annual rates.

The difference between precipitation weighted and regular temperature decreases linearly from 1.6 $\pm$ 0.5 K 12 kyr ago to 0.7 $\pm$ 0.4 K 4 kyr ago, and remains at this value for the last 4 kyr. This indicates that the temperature recorded in Greenland ice cores has been warm biased throughout the Holocene, caused only by changes in the seasonality of precipitation. These changes are the result of a response in atmosphere and ocean circulation to the orbital forcing applied.

This should be taken into account when calculating the temperature from the δ signals measured in the ice cores. This temperature could be explained as a superposition of the 'real' decrease in temperature and a bias, depending of the age of the ice.

Although the model produces a realistic temperature response, it should be noted that the boundary conditions are not changed in each experiment, e.g. the influence of changes in the major ice sheets have not been included. It is well documented that this have huge influence on surface albedo, atmospheric circulation and other factors (e.g. Renssen et al., 2005). Other limitations of the model are discussed in Chapter 2 and 6.

Chapter 5

Freshwater forcing

After an introduction to the possible trigger mechanisms, that could have caused the 8.2 kyr event, the experimental setup with ECBilt-CLIO is presented. The results using ECBilt-CLIO are followed by a discussion and conclusion on the subject.

5.1 The 8.2 kyr event

δO^{18} records from Greenland spanning the Holocene and last glacial period show abrupt climate changes, the so-called Dansgaard-Oeschger (D-O) events, during the glacial period (Dansgaard et al., 1993 and Grootes et al., 1993). The temperature change in Greenland during the D-O events has been estimated to range from 9 to 16 K (Lang et al., 1999), and it is believed that the trigger for such events is changes in the THC, thereby altering the heat transport by the ocean (Ruddiman and McIntyre, 1981). When the THC is active, heat is transported to high northern latitudes, and a shutdown (or reduction) of the THC would cause this region to cool substantially, and at the same time warm the SH by trapping heat (Stocker and Johnsen, 2003, and references therein).

Ice core records of δD from Antarctica show less abrupt changes in temperature (Johnsen et al., 1972), although smaller warmings and coolings are found during the last glacial period. The warmings and coolings are in antiphase and lag the signals recorded in Greenland ice cores. It has been proposed that this difference in amplitude, phase and delay in the response between the Greenland and Antarctic ice cores indicates that the climate in the north polar region leads that of the SH (Stocker and Johnsen, 2003).

In contrast to the ice core signals during glacial periods, the Holocene climate varies much less (Dansgaard et al., 1993, and Grootes et al., 1993). Johnsen et al. (2001) have used GRIP δO^{18} and borehole thermometry to calculate the temperature change on Summit, Greenland for the Holocene and last glacial period, shown in figure 5.1. The temperatures in the LGM

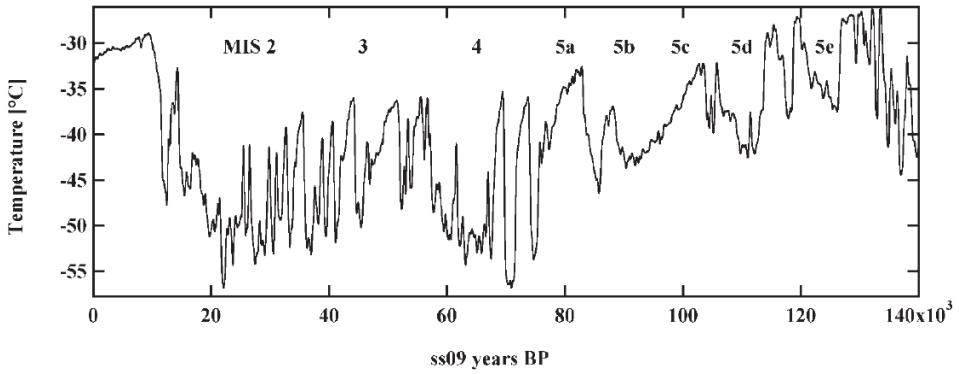

Figure 5.1: *Past temperature changes for Summit, Greenland, based on GRIP δO^{18} and borehole thermometry calibrations. From Johnsen et al. (2001).*

are about 20 K colder than those of today, and the D-O events discussed above are dominant between 80 to 15 kyr ago.

Where fluctuations of 5-7‰ in δO^{18} during last glacial are common, the largest excursion in Greenland ice cores during the Holocene is ∼2‰, found 8.2 kyr ago (von Grafenstein et al., 1998). This cooling has been detected in many other indicators in the Greenland ice cores, such as methane, dust, salt and precipitation rates (Alley et al., 1997, Blunier et al., 1995, and Chapellaz, 1997), and in cores from many other locations, particularly Europe (von Grafenstein et al., 1998) and the NA, but also indications of sudden changes in atmospheric circulation in Africa and Asia have been reported (Gasse and Van Campo, 1994 and Gasse, 2000), indicating that the 8.2 event was not restricted to the NA and north polar region.

It is believed that the 8.2 kyr event seen in figure 5.2 is caused by freshwater discharges, decreasing the strength of the THC with similar (but opposite in sign and smaller) responses as for the D-O events. The freshwater originates from the melting of the Laurentide ice sheet, and after being collected in large reservoirs, sudden drainage could account for such freshwater discharges (von Grafenstein et al., 1998).

In the model simulations described in the following section, the amount of freshwater has been kept fixed at $4.73 \times 10^{14}\mathrm{m}^3$, based on geological estimates of $5 \times 10^{14}\mathrm{m}^3$ (von Grafenstein et al., 1998)[1].

[1] $4.73 \times 10^{14}\mathrm{m}^3$ is used since 0.75 Sv over 20 years yields this number.

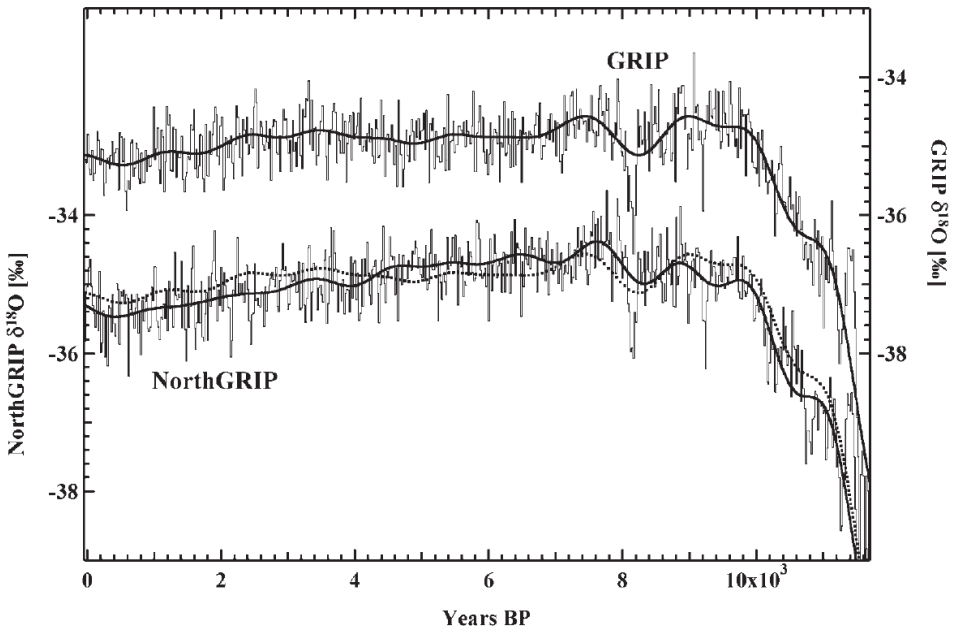

Figure 5.2: *20-year resolution of δO^{18} profiles from GRIP and NGRIP. The solid curves represent a 1 kyr low-pass filtered version of the data. The dotted curve is the GRIP 1 kyr low-pass data shown together with the NGRIP data. The 8.2 kyr event is clearly evident in both ice core signals. From Johnsen et al. (2001).*

5.2 The experimental setup

Using the spin-up state described in Chapter 3, experiments have been performed with ECBilt-CLIO forcing the model with freshwater pulses released at different locations in the NA. The total amount of freshwater released has been kept fixed, but the time over which the forcing is applied has been varied, with varying intensity of the freshwater discharge as a consequence.

Since the spin-up state from which the experiments are run uses present-day orbital forcing, it has been examined to what extent the overturning circulation responds to different orbital forcings during the Holocene. In figure 5.3 the maximum MOC for the four forcing experiments discussed in Chapter 4 is plotted, and the fluctuations in the strength of the overturning circulation are very similar for all experiments, varying between 28 and 30 Sv. Comparing the results of typical freshwater forcing experiments (e.g. figure 5.5), it is seen that the influence of orbital forcing on overturning circulation is very small, compared to that of freshwater forcings. Based on this argument, the present-day orbital forcing used in the spin-up state has not been altered when running the model with the freshwater forcing

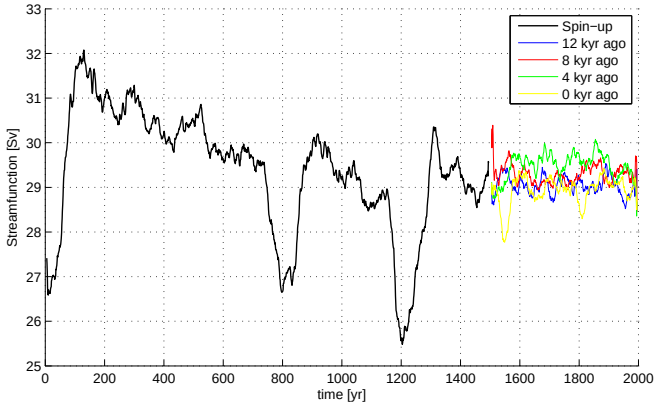

Figure 5.3: *Maximum MOC for the spin-up run followed by the different orbital forcing experiments plotted against time. The curves has been smoothed by 30 years of running mean.*

described in this section.

In ECBilt-CLIO each land area is coupled to an ocean grid cell through the land-sea mask given in figure 2.1. The hosing of freshwater is written into the code by adding extra run-off into the desired sea-mask in each time step, and the freshwater is then spread out in the oceans by the ocean circulation and mixing processes. As a consequence the freshwater is not released in a single grid cell, but distributed evenly over the amount of ocean grid cells that belongs to the given land-sea mask.

In the first two experiments, freshwater has been released in the Labrador Sea (land-sea mask M, hereafter referred to as experiment A) and the NA off the coast of Scandinavia (land-sea mask F, experiment B), and in both cases a 0.75 Sv freshwater pulse lasting 20 years, was hosed into the ocean. The model was then run another 500 years in order to catch the difference in response to such forcings[2]. Although the setup in experiment A is most likely to explain the mechanisms causing the 8.2 kyr event (see section 5.4), experiment B gives an insight to the model response to freshwater forcings at different locations.

In figure 5.4 the freshwater flux at the ocean surface is plotted for the two experiments at a time when the hosing occurs. The freshwater flux for experiment A is more intense but distributed over a smaller area (fewer grid cells) than for experiment B. Note that the freshwater input in experiment B is spread out from the Barents Sea in the north to the coast of Spain in

[2]In Chapter 3, it was found that the ocean spin-up time is around 700-800 years, but typical freshwater experiments show little to no variation in climate 300 years after a given forcing was applied (e.g. figure 5.5).

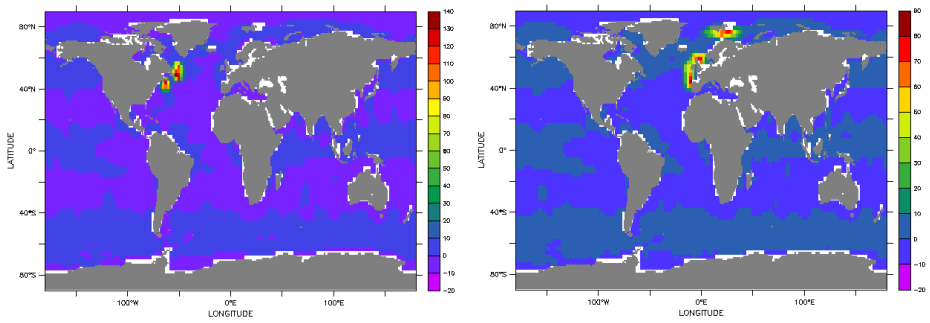

Figure 5.4: *Annual mean freshwater flux at the ocean surface for experiment A and B in [Sv].*

the south.

To check the stability in the response three realizations of experiment A has been performed (experiments A1, A2 and A3). In each case, the initial conditions are perturbed by letting the experiments start from the spin-up state with 5 year intervals.

The last set of experiments, A_{10}, A_{20} and A_{50}, uses the same setup as experiment A, but the time over which the pulse lasts is set to 10, 20 and 50 years, and since the total amount of freshwater release is fixed, the strength of the pulse becomes 1.5, 0.75 and 0.3 Sv respectively.

Analyzing and comparing the results to data from different ice and sediment cores will indicate, which of the configurations are most likely to explain the 8.2 kyr event.

5.3 Results

The results for the three sets of experiments are presented in the following section, mainly focusing on the response of the maximum MOC in the Atlantic Ocean and (sea)surface temperature to the forcings applied.

The maximum MOC is ∼29 Sv when the system is in statistical equilibrium given by the the spin-up state, and when freshwater is released, the maximum MOC decreases as long as the forcing is applied (figure 5.5 left). In experiment A the maximum MOC decreases quickly to a minimum of 21 Sv and increases gradually after 20 years of forcing and after 125 years it has reached the same level as before the forcing was applied. In experiment B the decrease persists 25 years after the forcing was applied, reaching 20 Sv before it starts to increase again and it takes 200 years to reestablish at 29 Sv.

The associated annual mean temperature response in a northern NA, Greenland and north polar region confined by the boundaries 90-0°W and

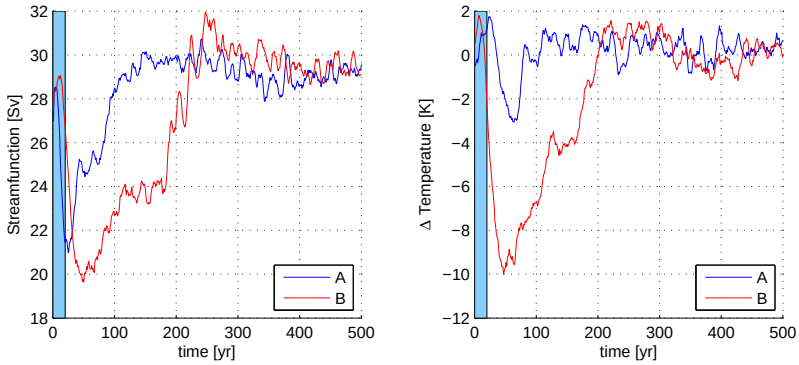

Figure 5.5: *Maximum MOC (left) and NA annual mean surface temperature response (right) plotted as anomalies from the mean temperature in the spin-up experiment for experiments A and B, smoothed by 10 years of running mean. The blue shading marks the time when the freshwater forcing was applied.*

60-90°N (hereafter referred to as 'NA temperature', figure 5.5 right) shows perturbations of -3 K at year 60 in experiment A, whereas the temperature response in experiment B is -10 K at year 50. In both experiments the temperature increases 1.9 K as an initial response to the freshwater discharge.

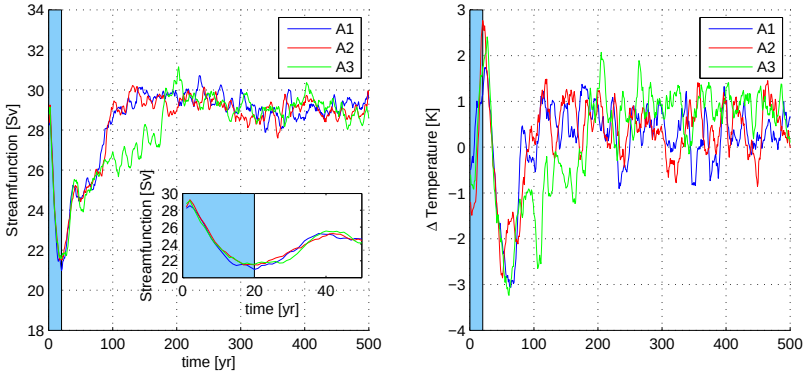

Figure 5.6: *Same as figure 5.5 but for experiments A1, A2, and A3. The embedded plot shows the first 50 years of the maximum MOC.*

The starting point of each ensemble run A1, A2 and A3 has been perturbed, and they all show very similar responses to the forcing applied (the same as in experiment A). In figure 5.6 the maximum MOC and NA temperature response are shown for the ensemble runs, and the resemblance is

striking, even during the time when the forcing is applied (embedded plot). The maximum MOC in experiment A1 and A2 (A3) is reestablished in year 125 (200), and the initial temperature increase and following decrease has almost the same amplitudes in all experiments. Furthermore, the Atlantic zonal mean anomalies in northward heat transport and SST (not shown) are much alike in all ensemble runs as well, and although the response in A3 is slightly different from A1 and A2, no important differences between the three are observed.

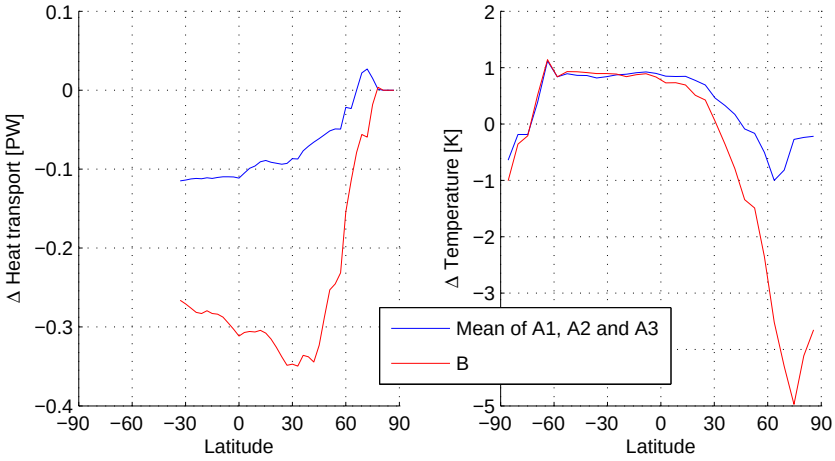

Figure 5.7: *Atlantic zonal mean anomalies in northward heat transport (left) and SST (right) for A_{ens} (blue) and B (red).*

Following the terminology used in section 5.1, the THC is *active* when no forcing is applied and *reduced* as a consequence of the release of freshwater. Letting the active mode be defined by temporal averages between year 450 and 470 in each experiment, and the reduced by a 20 year mean during the maximum excursion of MOC, the cooling of the NA can be explained by a decrease in northward oceanic heat transport. In the left panel in figure 5.7, the zonal mean anomaly of the latter shows negative values for the ensemble mean of experiments A1, A2 and A3 (A_{ens}) and B, thus affecting high latitude temperatures in the NH (figure 5.7, right). Again, the response is greatest in experiment B, with anomalies in heat transport and temperature of -0.35 PW at 45°N and -5.0 K at 85°N respectively. In experiment A_{ens} the heat transport anomaly gradually increases with latitude from -0.15 to +0.05 PW. Although the anomaly in experiment A_{ens} is much less than in B, in both cases less heat is transported north, causing the SH to warm ∼1 K from the Equator to 60°S in both experiments. It should also be noted that the heat transport anomaly is slightly positive around 70°N for A_{ens} partly counteracting the cooling of the high northern latitudes.

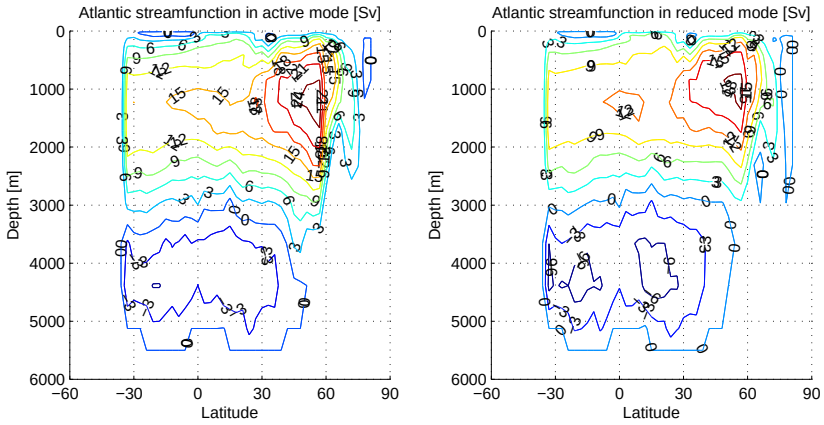

Figure 5.8: *Latitude-depth distribution of the MOC in the Atlantic for the active and reduced modes in* A_{ens}.

Since heat is advected in the Atlantic, the change in heat transport can be visualized by plotting the MOC in the two different modes (active and reduced, figure 5.8). In the active mode, heat is transported northward in the top 1,200 to 1,500 m with a maximum transport of 24 Sv[3], and this transport is reduced throughout the Atlantic Ocean with a maximum transport of 18 Sv. In the deep ocean the flow of AABW of 3 Sv in the active mode increases to 6 Sv in the reduced mode.

The amount and extent of sea-ice in the perturbed, cold state increases as seen in figure 5.9, especially the maximum sea-ice extent off the south-eastern and south-western coast of Greenland. The minimum sea-ice extend does not change much between the two states. Similar plots for the south polar region, show a small decrease in maximum sea-ice extent (not shown).

The three configurations, A_{10}, A_{20} and A_{50}, lead to different responses as seen in figure 5.10. In each of the experiments A_{10} and A_{20} the strength of the maximum MOC decreases as long as the forcing is applied, and the response is very similar, with a decrease of 8 Sv at run year 25 in both cases. In experiment A_{50}, the forcing persists for 50 years and throughout this period the maximum MOC is around 6 Sv lower than in the steady state.

The NH temperature exhibits the same features in experiments A_{10} and A_{20}, although the maximum temperature excursion is larger in experiment A_{10} than in A_{20} (-4 compared to -3 K). An initial increase in temperature is common for all three experiments, whereas the negative response at run year 50 only can be identified for A_{10} and A_{20}. In experiment A_{50}, the temperature drops -3 K at run year 80. It takes $\sim$ 150 years for both the

[3]The contours does not show the actual maximum MOC, but in figure 5.5 it is seen that the value is around 30 Sv.

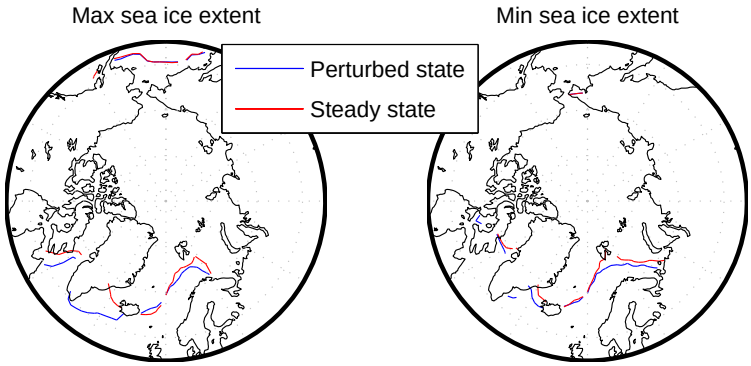

Figure 5.9: *Maximum (September) and minimum (March) sea-ice extent in the perturbed (blue) and steady (red) states for A_{ens}. Contour lines represents 20 cm sea-ice thickness.*

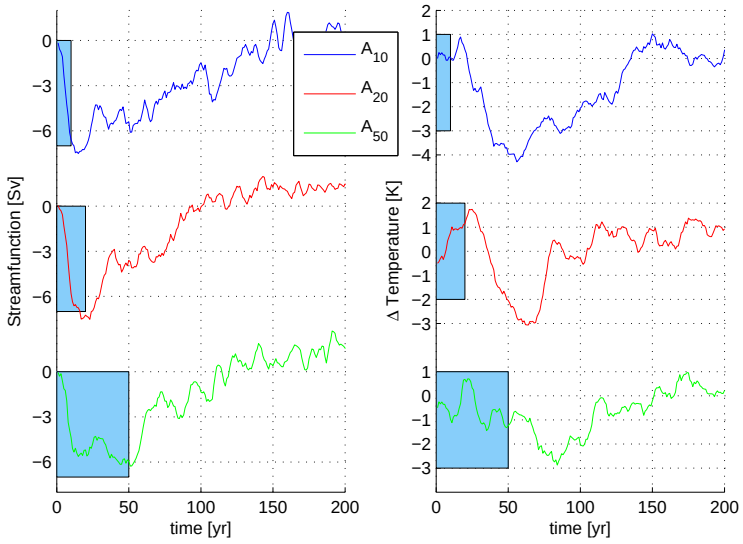

Figure 5.10: *Same as figure 5.5 but for experiments A_{10}, A_{20} and A_{50}.*

maximum MOC and the temperature to reach steady state values in all three experiments.

A comparison of the NA and SH temperature response to the forcing applied in experiment A_{ens} is given in figure 5.11. Both curves show an initial increase of 1.8-2 K, but where the NA temperature decreases after

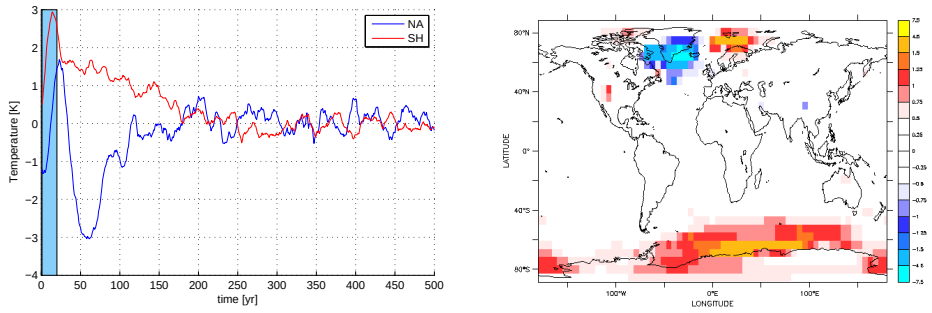

Figure 5.11: *Left: Average surface temperature response to the forcing applied in A_{ens} for the NA and SH, plotted as anomalies from the mean temperature in the spin-up experiment. Data has been smoothed by 10 years of running mean. Right: Surface temperature anomalies in K, again for A_{ens}. Note the non-linear scale.*

the forcing is shut off, the SH temperature is slowly restored. This warming lasts $\sim$ 200 years, and can in some way be explained by a bipolar seesaw mechanism trapping heat in the SH described earlier. In the right panel the trapping of heat in the SH can be visualized in a map showing temperature differences between the equilibrium steady state climate and the mean temperature during years of maximum excursion. The warming in the SH show an increase in temperature of 1-4.5 K distributed off the coast of Antarctica, mainly in the southern Atlantic and Indian Ocean. The increased sea-ice extent off the southern coast of Greenland can also be seen as a decrease in temperature.

Since Chapter 4 concluded that the precipitation weighted temperature calculated from the model results should be compared to data from Greenland ice cores, a comparison of the regular and precipitation weighted temperature has been carried out for four grid cells in central Greenland.

	P [°C]	S [°C]	S - P [K]
T_A	-27.0	-23.6	3.4 $\pm$ 0.6
T_{PW}	-23.3	-21.9	1.4 $\pm$ 0.4

Table 5.1: *Central Greenland regular (T_A) and precipitation weighted (T_{PW}) temperature in the perturbed (P) and steady (S) state and the difference between the two. All values are calculated for A_{ens}, and standard deviations are only shown for $S - P$ values.*

In table 5.1 the precipitation weighted temperature shows a 1.4 $\pm$ 0.4 K difference between the perturbed and steady state. On the other hand, the regular temperature difference is 3.4 $\pm$ 0.6 K indicating that the seasonality

of precipitation is shifted between the two states. Indeed, looking at figure 5.12 the summer and autumn precipitation ratios are 6 and 4% larger in the perturbed state than in the steady state, while the winter and spring precipitation ratios have decrease accordingly.

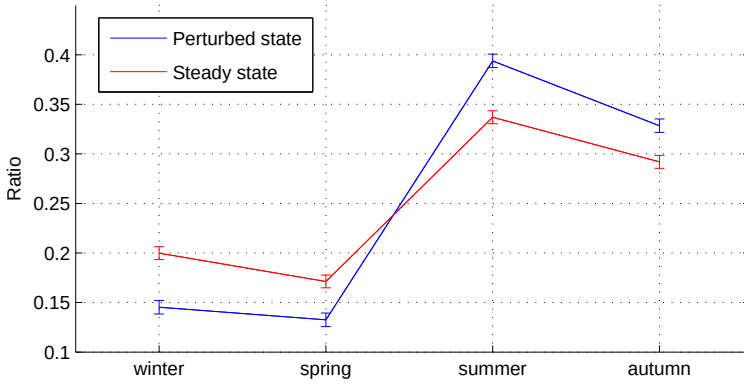

Figure 5.12: *Ratio of seasonal to total precipitation for the perturbed and steady state of A_{ens}. Error bars represent two standard deviations.*

5.4 Discussion

As was the case in Chapter 4, different studies on proxy data evidence and model simulations on the topic will be presented below.

5.4.1 Proxy data

The 8.2 kyr event has been observed in many indicators of climate, especially in the Greenland ice cores. Alley et al. (1997) used GISP2 ice core data to calculate the decrease in temperature to 6 $\pm$ 2 K and the approximate duration of the event was reportedly anything from 100 to 1,000 years. von Grafenstein (1998) found a 200 year negative excursion in a European sediment core coinciding with the δO^{18} excursion found in the GRIP core around 8.2 kyr ago and estimated the associated temperature drop in Greenland to 2.8 K.

Recent studies have shown that the event is observed as a 160.5 year period of reduced δ ratios, within which there is a 69 year period with significantly lower values than the early Holocene average, see figure 5.13 (Thomas et al., 2007). This is done by a collection of high-resolution chemistry and isotope records from Dye3, GISP2, GRIP, and NGRIP and the local temperature drop at the ice core sites is estimated to 3-8 K. Leuenberger et al.

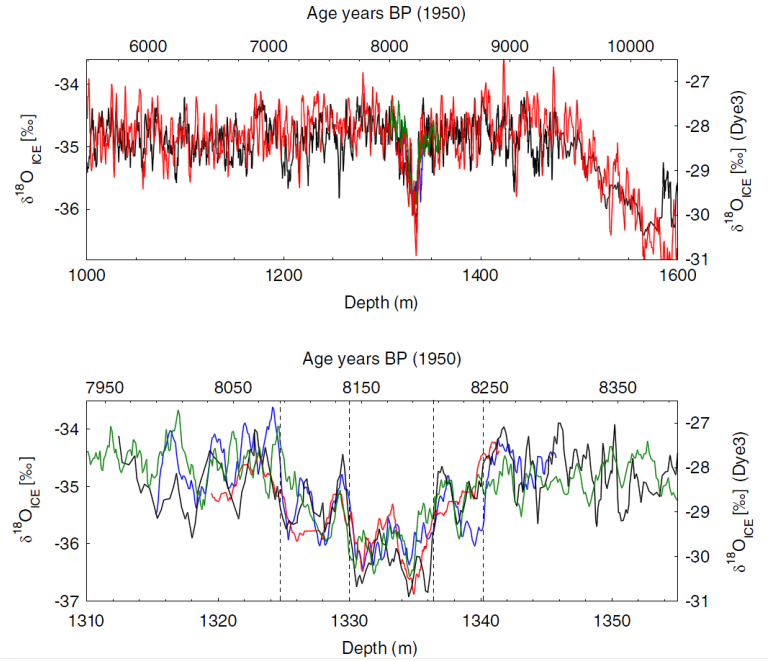

Figure 5.13: *δO^{18} ratios for GRIP (red), GISP2 (black), NGRIP (blue), and Dye 3 (green) plotted on the GRIP depth scale and GICC05 age scale. Curves in upper (lower) panel are smoothed by 20 (10) years of running mean. Dashed lines represents the onset and termination of the whole and central 8.2 kyr event. From Thomas et al. (2007).*

(1999) have performed similar studies on Greenland ice cores and found that the excursion in around 5.4 to 11.7 K. These values are somewhat larger than the estimated precipitation weighted temperature in central Greenland by the model (1.4 $\pm$ 0.4 K). Furthermore, the results presented in section 5.3 indicates that the actual decrease in temperature is higher than what is measured in the ice cores, given the shift in seasonality of precipitation and the difference between the regular and precipitation weighted temperature, i.e. the warm bias during the cooling event, is 2 $\pm$ 0.6 K.

Rohling et al. (2005) questioned the geographical extent of the rapid cooling event 8.2 kyr ago. They compared anomalies in climate proxies from locations around the globe and found that the event is most likely to be a superposition of a long-term cooling lasting from 8.6 to 8.0 kyr ago and the sudden cooling 8.2 kyr ago. Proxies showed less pronounced Indian and Asian monsoons, a temperature decrease at two sites in the Mediterranean Sea and one in Ireland, Germany and the Norwegian Sea, lower precipitation rates off the coast of Venezuela and the advance of Norwegian glaciers. Given the perturbed and steady state described in section 5.3, anomalies in tem-

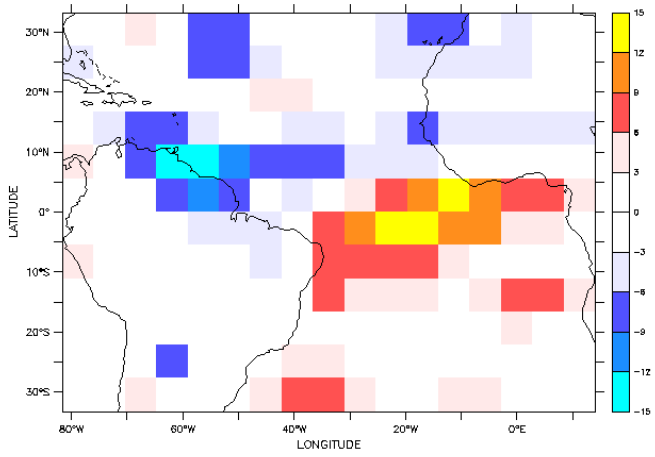

Figure 5.14: *Precipitation anomalies in the Atlantic tropics for the perturbed state of A_{ens}. Units are cm/yr.*

perature and precipitation for the regions given above have been compared to those examined by Rohling et al. (2005). No significant temperature signal was found in the model results in the different regions and only in the Mediterranean Sea and off the coast of Venezuela anomalies in precipitation was observed ranging from -8 to -16 cm/yr (figure 5.14). Rohling et al. (2005) attributed the aridity in some of the monsoon records to a decrease in the northward migration of the intertropical convergence zone. In the Atlantic the model results show an increase of precipitation close to the Equator, indicating a southward shift in the tropics (figure 5.14).

The duration of the event in all experiments were all around 150-200 years and it can be concluded, that the experiments performed are able to explain possible trigger mechanisms for the 8.2 kyr event. It is difficult to say which of the experiments A_{10}, A_{20} and A_{50} is most likely to explain the event, given their very similar response in both maximum MOC and NA temperature.

5.4.2 Other model studies

Renssen et al. (2001) has also used ECBilt-CLIO to perform freshwater forcing experiments. The spin-up state was reached using 8.5 kyr boundary conditions such as adjustments in insolation, GHG concentrations, surface albedo and surface height and following the terminology used in section 5.3 the experiments included A_{10}, A_{20}, A_{50} and A_{500} type setups. Examining the maximum MOC in the NA (between 60-80°N) they found that the A_{500} experiment resulted in very small perturbations, whereas the other three resulted in event-like weakenings of the maximum MOC. Moreover,

A_{10} resulted in a permanent weakening of the maximum MOC lasting for at least 1,000 years, while the A_{20} and A_{50} maximum MOC recovered to pre-perturbed values after 145 and 320 years respectively. They also found a shift in the main convection site from south of Svalbard to off the coast of Norway, an increase in sea-ice extent and a decrease in near-surface temperature over the Nordic Seas (5-10 K) and Greenland (2-5 K), all very close to what is reported in section 5.3. In a later study they performed 5 ensemble runs of A_{10}, A_{20} and A_{50} and found, that the maximum MOC recovered in all A_{50}, in three of A_{20} and in only one of the A_{10} experiments[4] (Renssen et al. 2002). They proposed that the likeliness of a maximum MOC recovery increases with the duration of the freshwater pulse. The positive ice-albedo feedback was proposed as a stabilizing factor resulting in increased recovery time.

Many other studies with EMICs and AOGMCs have been published on the topic over the past years, e.g. Manabe and Stouffer (1995), Alley et al. (1997), Wiersma and Renssen (2005), Long et al. (2006) and LeGrande et al. (2006, 2008). In a series of coordinated experiments the Coupled Model Intercomparison Project/Paleo-Modeling Intercomparison Project (CMIP/PMIP) committee has examined the THC response to a 0.1 and 1.0 Sv freshwater perturbation over the 50-70°N of the NA lasting 100 years and the associated climate changes using a broad spectrum of EMICs and AOGCMs, ECBilt-CLIO included (Stouffer et al., 2006). In all models the THC weakened rapidly; the maximum MOC decreased 6 Sv for the ensemble mean for all models included, with a cooling of the NH and a less intense warming of the SH as a consequence. In some of the models the THC recovered whereas it remained in a reduced mode in others. Stouffer et al. (2006) proposed three possible explanations for this inconsistency 1) the reduced mode is unstable, 2) the duration of the freshwater pulse is too short, or 3) the intensity of the pulse is too small to reach a stable reduced mode. Considering the results of Renssen et al. (2002) a combination of 2) and 3) seems to apply for ECBilt-CLIO since it can exhibit steady-state modes lasting more than 1,000 years. In general, the ECBilt-CLIO response in maximum MOC of 7-8 Sv is in reasonable agreement with what is found using other models.

The control runs, i.e. experiments where the models are in statistical equilibrium, showed very different intensity of the THC among the models participating in the CMIP/PMIP analysis. Stouffer et al. (2006) divided the models into three groups, a) models exhibiting strong and large multidecadal variations in THC (maximum MOC 20-30 Sv), b) models with less intense and less variation in the THC (maximum MOC 13-20 Sv) and c) less complex EMICs with little or no variation in THC. As mentioned in Chapter 2 and 3 ECBilt-CLIO is relatively close to AOGCMs (Claussen et al., 2002) and

[4]In this context, no recovery represents a recovery time $>$ 500 years.

the simulation of the THC belongs to the a)-type models, as the only EMIC partitioning in the comparison analysis. The intensity of the THC in the unperturbed state in the experiments described in section 5.3 is in the higher end, with maximum MOC $\sim$ 29 Sv.

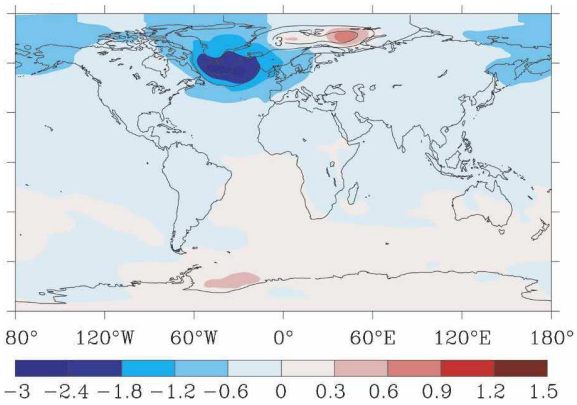

Figure 5.15: *The ensemble mean anomalies of surface air temperature in K between the 0.1 Sv and control experiment (color shades) and standard deviation among model simulations (solid lines). From Stouffer et al. (2006).*

Comparing the surface temperature change from the results from experiment A_{ens} (figure 5.11, right panel) to the 0.1 Sv experiment from the CMIP/PMIP analysis (figure 5.15) the resemblance is striking. The warming of Southern Ocean is clearly evident in both figures, as well as a surface temperature dipole in the northern NA with a warming over the Barents and Nordic Seas and a cooling south of Greenland. This dipole is probably closely related to the shift in main convection sites reported by Renssen et al. (2001) and this pattern might be a key indicator of future changes in the THC. It should be noted that the temperature change is much higher in the results from experiment A_{ens} (4-8 K) compared to those in figure 5.15 (1-3 K), but given the difference in intensity of the forcing applied (0.1 Sv for 100 years and 0.75 Sv for 20 years) this is what could be expected.

Ganopolski and Rahmstorf (2001) have used an EMIC (CLIMBER-2) to perform a stability analysis with LGM boundary conditions and found that the boundary conditions play an important role for the stability of the THC. Since the boundary conditions used in this thesis differs from what is used by Renssen et al. (2001, 2002) as already described, this could explain why all ensemble runs show a restoring trend in the maximum MOC, while Renssen et al. (2002) found various responses to the same type of forcing applied. It seems that the present day boundary conditions lead to a more unstable reduced mode and hence the THC restores more easily after a given forcing has been applied, when compared to early Holocene boundary conditions.

This aspect could be useful in future climate research.

It is widely accepted that the 8.2 kyr event is caused by freshwater discharges from the melting of the Laurentide ice sheet, as discussed above. Results from experiment B also confirms that this setup results in an unrealistic temperature response of -10 K in the NA.

In all experiments performed with ECBilt-CLIO the temperature increases 1-2 K as an initial response to the freshwater discharge, but the mechanisms causing this increase is not easily understood and more work is needed to explain this response.

The antiphase response in temperature of the NA and SH has been studied intensely by e.g. Stocker (1998) and Stocker and Johnsen (2003). In the latter study, they used a very simple model to explain the 'seesaw-like' interconnection between the hemispheres also seen in figure 5.11, left panel. The input for the model was GRIP δO^{18} records and the model then reproduced a lagged 'SH temperature' response and they found a delay of $\sim$ 1,120 years yielded the most realistic SH temperatures when compared to the δO^{18} record from the Antarctic ice core Byrd. This delay represents the overturning timescales of the oceans meaning that a NH climatic event will be delayed by this mechanism. In figure 5.11 left panel, no such delay is seen; the SH responds as quickly as the NA temperature to the forcing applied. Since heat is advected in the Atlantic Ocean by the surface water a weakening of the circulation causes heat to be trapped in the SH rather quickly. Barron and Kara (2008) has estimated the SST time scale to range between 10 to 30 days depending on latitude and this could explain the 'missing' delay in SH temperature response.

5.5 Conclusion

A rapid cooling event spanning 160 years is found in proxy data 8.2 kyr ago, and the event is particularly evident in Greenland ice cores. The release of melt water from the Laurentide ice sheet is believed to have caused changes in the THC, thereby changing the climate state. Model simulations confirms that such a freshwater pulse is able to account for the cooling found in the Greenland ice cores.

In the present study the intermediate complexity model ECBilt-CLIO was used to carry out experiments simulating the release of freshwater. The water was added to the run-off from land areas close to the Labrador Sea, the amount added was based on geological evidence, and the time over which the water was released was varied. Furthermore an ensemble mean of three experiments was performed in order to check the variability in the climate response to such forcings.

All experiments showed consistent results, with minor differences in the response to a given forcing applied and the most prominent changes in the climate during the cooling event were

- a decrease in the maximum MOC of 6 to 7 Sv
- a weakening of the northward heat transport in the Atlantic, trapping heat in the SH
- a 3-4 K decrease in the NA temperature
- expanding (and less pronounced retreating) sea-ice off the southern coast of Greenland (around Antarctica)
- a bipolar shift in temperature with increased temperatures at the Barents Sea and decreased temperatures off the southern coast of Greenland
- an increase in Southern Ocean temperatures of 1-4.5 K
- a shift toward more summer and autumn precipitation and less during winter and spring
- a difference between the decrease in regular and precipitation weighted temperature in central Greenland of 3.4 ± 0.6 and 1.4 ± 0.4 K respectively

It was found that the climate in the perturbed state was comparable to proxy data from Greenland, although the decrease in temperature was in the lower end of what is estimated from ice core data. However, previous model studies have very similar results compared to what is presented in the list above.

Moreover, the results indicated that the temperature excursions found in ice cores are warm biased 2.0 ± 0.6 K, i.e. the cooling event might be even more extreme than what the measured δO^{18} signals show.

The duration of the event (150 years) was in good agreement both with proxy data and previous model results.

As was the case with the orbital forcing experiments, no changes in boundary conditions were taken into account.

Chapter 6

Final conclusion

The focus of this thesis has been on the study of two main aspects; a) seasonality changes of precipitation during the Holocene in Greenland and the influence of this on the precipitation weighted temperature, and b) possible explanations of the 8.2 kyr event. This has been done forcing the comprehensive EMIC ECBilt-CLIO with a) Holocene orbital parameters and b) freshwater discharges in the NA and the main results are;

a) the precipitation weighted temperature in Greenland was 1.6 ± 0.5 to 0.7 ± 0.4 K higher than the regular temperature during the Holocene, with a shift occurring around 4 kyr ago. This bias is caused by a shift toward greater summer precipitation rates, a result of changes in the orbital parameters

b) the 8.2 kyr event can be explained by the release of freshwater into the NA. In the model, such forcings set off a cooling event across the northern NA and north polar region, with a decrease in temperature of 3-4 K. In central Greenland the precipitation weighted temperature excursion was 2 ± 0.6 K higher than the regular temperature, indicating that the event might have been more extreme than what is found in the ice cores

In general a reasonable correspondence was found between the results and proxy data and previous model studies. Assuming that the modeled climate responds correctly, the results give confidence in the concept of the influence of changing orbital parameters on the precipitation weighted temperature and the explanation of the 8.2 kyr event.

In Chapter 2 the physics and parameterizations included in ECBilt-CLIO were described. One should keep in mind, that the results depend strongly on the ability to represent the atmosphere and ocean correctly. The simple hydrological cycle, the parameterization of clouds and vertical mixing in the ocean, flux-corrections etc. are all examples of tunable parameters each

influencing the output of the model. Although the results are in reasonable accordance with proxy data, this should always be considered.

6.1 Outlook

As described in section 4.5, many factors have the potential to change the seasonality of precipitation at high latitudes, changes in orbital parameters being one of them. Other mechanisms that are possible to incorporate in the model, could be changes in boundary conditions throughout the Holocene such as GHG, vegetation types and the extent of the major ice sheets including changes in the orography. These improvements could lead to a more sophisticated picture of the Holocene climate, thus affecting the results from similar experiments as performed in Chapter 4 and 5. Such improvements could be achieved by performing the experiments with the newest version of ECBilt-CLIO, called LOVECLIM which includes dynamical vegetation and ice sheet components.

It would also be of interest to perform a transient experiment throughout the Holocene, with changes in orbital parameters. This might shed more light on the changes in the seasonality of precipitation. Likewise, performing more ensemble runs of the freshwater forcing experiments could to some extent validate the results and experiments with varying total amount of freshwater release would be of interest.

Acknowledgments

First of all, I would like to thank the Centre for Ice and Climate, Niels Bohr Institute, University of Copenhagen, for providing excellent conditions for their students.

Secondly, my supervisor Peter L. Langen, for introducing me to the field of climate modelling, for the inspirational supervision and for always taking the time to explain and discuss different aspects, no matter how simple or complex they might be. His help has been of tremendous importance.

Thirdly, the guys from the office and 'the Villa' for the endless discussions and laughs. Without their help, ideas and company, the last year would have been much more difficult and a lot less fun. A special thank goes to Joakim R. Nielsen and Brian Sørensen for proof reading; I will hold them responsible for any typos that may occur.

Til sidst vil jeg gerne takke min familie og venner for deres støtte og forståelse. Af størst betydning har dog været Julies evige tro på mig.

Peter Riddersholm Wang

Appendix A

List of Symbols

a	radius of the Earth
A	area
A	lead fraction
AABW	Antarctic Bottom Water
(AO)GCM	(Atmosphere Ocean) General Circulation Model
c_p	specific heat capacity
C	constant calculated from the heat budget of open water
C	heating of the atmosphere by condensation of water vapor
CCM	Community Climate Model
CLIO	Coupled Large-scale Ice Ocean
d	deuterium excess
D	divergence of the horizontal wind
D	horizontal diffusivity
EBM	Energy Balance Model
EMIC	Earth Model of Intermediate Complexity
f_o	Coriolis parameter at 45°N and S
f	Coriolis parameter
F_{dS}	scalar correction term
$\mathbf{F}_{du}$	correction term for the small scale viscosity
F_i	heat flux within the ice
F_o	heat flux from the ocean to the ice
F_T	advection of temperature by the ageostrophic wind
$F_{v\theta}$	scalar correction term
F_ζ	ageostrofic correction factor
$\mathbf{F}$	internal force per unit area
g	gravitational constant
$G(h)$	correction term
GHG	greenhouse gas
h	ice thickness
i	i'th grid cell

k_d	tunable coefficient for diffusion
k_R	Rayleigh damping coefficient
k	thermal conductivity
L_i	heat of fusion of ice
LOVECLIM	LOchŰVecode-Ecbilt-CLio-agIsm Model
m	mass of snow and ice per unit area
MOC	Meridional Overturning Circulation
NA	North Atlantic
NADW	North Atlantic Deep Water
NH	northern hemisphere
p	pressure
P	perturbed state
P	precipitation
q_a	water content in the moist layer
q_{max}	integrated saturation specific humidity below 500 hPa
Q	diabatic heating
R	gas constant
S_ϑ	rate of change of ϑ due to thermodynamic effects
S	salinity
S	steady state
SH	southern hemisphere
SST	sea surface temperature
SWI	stable water isotopes
t	time
T	temperature
THC	thermohaline circulation
$\mathbf{u}$	horizontal velocity
$\mathbf{V}_a$	transport velocity
$\mathbf{V}_\psi$	rotational component
w	vertical velocity
x	x-coordinate, towards east
y	y-coordinate, towards north
z_h	topografic height
z	z-coordinate, upwards
δ	ratio of SWI in a sample to that of SMOW
η	sea-surface elevation
Γ	unit step function
λ	longitude
ω	vertical velocity
ϕ	geopotential
ϕ	latitude
$\phi(A)$	decreasing function defined for $0 \leq A \leq 1$
ψ	stream function

ρ	density
σ	static stability
σ	Stefan-Boltzmann constant
τ_a	force per unit area from the air
τ_w	force per unit area from the water
θ	potential temperature
ϑ	any physical variable
ζ	vertical component of the vorticity vector

Bibliography

[1] Alley, R. B., Mayewski, P. A., Sowers, T., Stuiver, M., Taylor, K. C., and Clark, P. U. *Holocene climatic instability: A prominent, widespread event 8200 yr ago*, Geology, vol. 25 no. 6, p. 483 - 486, 1997.

[2] Alley, R. B., et al. *Abrupt climate change*, Science, vol. 299, pp. 2005 - 2010, 2003.

[3] Andersen, C., Koc, N., Jennings, A., and Andrews, J. T. *Nonuniform response of the major surface currents in the Nordic Seas to insolation forcing: Implications for the Holocene climate variability*, Paleoceanography, 19, PA2003, 2004.

[4] Ausustin, L. et al. *Eight glacial cycles from an Antarctic ice core*, Nature. 429(6992) 623-8, 2004.

[5] Barron, C. N. and Kara, A. B. *Time Scales for SST over the Global Ocean*, Submitted to Geo. Res. Letters., 2008. See `http://www.ssmi.com/papers/gentemann/barron_submitted.pdf`.

[6] Berger, A. L. *Long-term variations of daily insolation and Quaternary climatic changes*, J. of Atmospheric Sciences vol. 35, pp. 2362 - 2367, 1978.

[7] Blunier, T., Chappellaz, J., Schwander, J., Stauffer, B., and Raynaud, D. *Variations in atmospheric methane concentration during the Holocene epoch*, Nature 374, 46 - 49, 1995.

[8] Bond, G., Broecker, W., Johnsen, S., McManus, J., Labeyrie, L., Jouzel, J.,and Bonani, G. *Correlations between climate records from North Atlantic sediments and Greenland ice*, Nature 359, 311 - 313, 1992.

[9] Braconnot, P., Marti, O., Joussaume, S., and Leclainche, Y. *Ocean Feedback in Response to 6 kyr BP Insolation* Journal of Climate, Article: pp. 1537 - 1553, 2000.

[10] Budyko, M.I. *The effect of solar radiation variations on the climate of the earth*, Tellus vol. 21, pp. 611 - 619, 1969.

[11] Cai, M. *Dynamical greenhouse-plus feedback and polar warming amplification. Part I: A dry radiative-transportive climate model*, Climate Dynamics 26: 661 - 675, 2006.

[12] Chappellaz, J *Changes in the atmospheric CH4 gradient between Greenland and Antarctica during the Holocene*, J. Geophys. Res., 102, 15,987Ű15,997, 1997.

[13] Chassignet, E. P., and Verron, J. *Ocean Modeling and Parametrization*, Kluwer Acedemic Publishers, 1998.

[14] Claussen., M., et al. *Earth system models of intermediate complexity: closing the gap in the spectrum of climate system models*, Climate Dynamics 18: 579 - 586, 2002.

[15] Collins, W. D., Bitz, C. M., Blackmon, M. L., Bonan, G. B., Bretherton, C. S., Carton, J. A., Chang, P., Doney, S. C., Hack, J. J., Henderson, T. B., Kiehl, J. T., Large, W. G., McKenna, D. S., Santer, B. D., and Smith, R. D. *The Community Climate System Model: CCSM3*, For JJLI CCSM Special Issue, 2006, Model available at `http://www.ccsm.ucar.edu/models/ccsm3.0/`

[16] Dansgaard, W. *Stable isotopes in precipitation*, Tellus, vol. 16, 1964.

[17] Dansgaard, W., White, J. W. C., and Johnsen, S. J. *The abrupt termination of the Younger Dryas climate event*, Nature 339, 532 - 534, 1989.

[18] Dansgaard, W., et al. *Evidence for general instability of past climate from a 250-kyr icecore record*, Nature, 364, 218 - 220, 1993.

[19] Gasse, F., and Van Campo, E. *Abrupt post-glacial climatic events in west Asia and North Africa monsoon domains*, Earth Planet. Sci. Lett., 126, 435 - 456, 1994.

[20] Gasse, F. *Hydrological changes in the African tropics since the Last Glacial Maximum*, Quat. Sci. Rev., 19, 189 - 211, 2000.

[21] Goosse, H., and Fichefet, T. *Importance of ice-ocean interactions for the global ocean circulation: A model study*, J. Geophys. Res. vol. 104, 1999, pp 23,337 - 23,355.

[22] Goosse, H., et al. *Description of the CLIO model version 3.0*, Scientific Report, 2000a.

[23] Goosse, H., et al. *CLIO 3.0: Description of some routines*, Scientific Report, 2000b.

[24] Goosse, H., Selten, F. M., Haarsma, R. J., and Opsteegh, J. D. *Decadal variability in high northern latitudes as simulated by an intermediate-complexity climate model*, Annals of Glaciology, Volume 33, Number 1, pp. 525 - 532(8), January 2001.

[25] Gregory, J. M. et al., *A model intercomparison of changes in the Atlantic thermohaline circulation in response to increasing atmospheric CO2 concentration*, Geophysical Research Letters, vol. 32, 2005.

[26] Grootes, P. M., et al. *Comparison of oxygen isotope records from the GISP2 and GRIP Greenland ice cores*, Nature 366, 552 - 554, 1993.

[27] Haarsma, R. J., Selten, F. M., Opsteegh, J. D., Lenderink, G., and Liu, Q. *ECBilt. A coupled Atmosphere Ocean Sea-ice model for climate predictability studies*, Technical Report, 1998.

[28] Holton, J., R. *An introduction to dynamic meteorolog*, Academic Press Inc., 3rd edition.

[29] Solomon, S., Qin, D., Manning, M., Chen, Z., Marquis, M., Averyt, K. B., Tignor M., and Miller, H. L. (eds.) *IPCC, 2007. Climate Change 2007: The Physical Science Basis. Contribution of Working Group I to the Fourth Assessment Report of the Intergovernmental Panel on Climate Change*, Cambridge University Press, Cambridge, United Kingdom and New York, NY, USA, 996 pp, 2007.

[30] Dansgaard, W., Johnsen, S. J. *Evidence for general instability of past climate from a 250-kyr ice-core record* Nature, 364, 218 - 220, 1969.

[31] Johnsen, S. J., Dansgaard, W., Clausen, H. B., and Langway, C. C. *Oxygen isotope profiles through the Antarctic and Greenland ice sheets*, Nature, 235, 429 - 434, 1972.

[32] Johnsen, S.J., Clausen, H.B., Dansgaard, W., Fuhrer, K., Gundestrup, N., Hammer, C.U., Iversen, P., Jouzel, J., Stauffer, B., Steffensen, J.P. *Irregular glacial interstadials recorded in a new Greenland ice core*, Nature 359, 311 - 313, 1992.

[33] Johnsen, S.J., Dahl-Jensen, D., Dansgaard, W., and Gundestrup, N. *Greenland palaeotemperatures derived from GRIP bore hole temperature and ice isotope profiles*, Tellus 47B, 624 - 629, 1995.

[34] Johnsen, S.J. et al. *Diffusion of stable isotopes in polar firn and ice: the isotope effect in fin diffusion*, Phys. Ice Core Records, 2000.

[35] Johnsen, S. J., Dahl-Jensen, D., Gundestrup, N., Steffensen, J. P., Clausen, H. B., Miller, H., Masson-Delmotte, V., Sveinbjörnsdottir, A. E. and White, J. *Oxygen isotope and palaeotemperature records from six*

Greenland ice-core stations: Camp Century, Dye-3, GRIP, GISP2, Renland and NorthGRIP J. Quaternary Sci., vol. 16, pp. 299 - 307, 2001.

[36] Kantha L. H., and Clayson C. A. *Numerical Models of Oceans and Oceanic Processes*, 3rd edition, Academic Press, 1999.

[37] Kiehl, J. T.,Hack, J. J., Bonan, G. B., Boville, B. A., Briegleb, B. P., Williamson, D. L., Rasch, P. J. *Description of the NCAR Community Climate Model (CCM3)*, Technical Report TN-420, CGD, National Center for Atmospheric Research, 1996.

[38] Knauss, J. A., *Introduction to Physical Oceanography*, 2nd edition, Prentice Hall, 1997.

[39] Knutti, R. J. Flückiger, Stocker, T. F., and Timmermann, A. *Strong hemispheric coupling of glacial climate through freshwater discharge and ocean circulation*, Nature 430, 2004, pp. 851 - 856.

[40] Krinner, G., Genthon, C., and Jouzel, J. *GCM analysis of local influences on ice core δ signals*, Geophysical Research Letters, vol. 24, no. 22, 1997.

[41] Krinner, G. and Werner, M. *Impact of precipitation seasonality changes on isotopic signals in polar ice cores: a multi-model analysis*, Earth Planet Sci Lett 216, 525 - 538, 2003.

[42] Lang, C., Leuenberger, M., Schwander, J., and Johnsen, S. J. *16C rapid temperature variation in central Greenland 70,000 years ago*, Science, vol. 286, 934 - 937, 1999.

[43] Langen, P. L. *Polar amplification of surface temperature change in a warming climate*, Ph.D. Thesis, 2005.

[44] Langen, P. L., and Vinther, B. M. *Response in atmospheric circulation and sources of Greenland precipitation to glacial boundary conditions*, Climate Dynamics 10, 2008.

[45] Leuenberger, M. C., Lang, C. and Schwander, J. *$\delta^{15}N$ measurements as a calibration tool for the paleothermometer and gas-ice age differences: a case study for the 8200 BP event on GRIP ice*, Journal of Geophysical Research 104D, pp. 22163 - 22170, 1999.

[46] LeGrande, A. N., Schmidt, G. A., Shindell, D. T., Field, C. V., Miller, R. L., Koch, D. M., Faluvegi, G and Hoffmann, G. *Consistent simulations of multiple proxy responses to an abrupt climate change event*, PNAS, January 24, vol. 103, no. 4, 837 - 842, 2006.

[47] LeGrande, A. N. and Schmidt, G. A. *Ensemble, water isotopeÜenabled, coupled general circulation modeling insights into the 8.2 ka event*, Paleoceanography, vol. 23, 3207, 2008.

[48] Liu, Z., Brady, E., and Lynch-Stieglitz, J. *Global ocean response to orbital forcing in the Holocene*, Paleoceanography, 18(2), 1041, 2003.

[49] Long, A. J., Robertsa D. H., Dawson, B. *Early Holocene history of the west Greenland Ice Sheet and the GH-8.2 event*, Quaternary Science Reviews 25, 904 - 922 2006.

[50] Loutre, M. F., D. Paillard, F. Vimeux, E. Cortijo *Does mean annual insolation have the potential to change the climate?* Earth and Planetary Science Letters 221, 2004.

[51] Manabe, Syukuro, et al. *Simulated Climatology of General Circulation with a Hydrologic Cycle*, Monthly Weather Review 93, 769 - 98, 1965.

[52] Manabe, S. and Stouffer, R. J. *Simulation of abrupt climate change induced by freshwater input to the North Atlantic Ocean.* Nature 378, 165 - 167, 1995.

[53] Masson-Delmotte, V., Cheddadi, R., Braconnot, P., Joussaume, S., and Texier, D. *Mid-Holocene climate in Europe: What can we infer from PMIP model-data comparisons*, Clim. Dyn., 15, 163 - 182, 1999.

[54] Masson-Delmotte, V., et al. *Holocene Climate Variability in Antarctica Based on 11 Ice-Core Isotopic Records*, Quaternary Research 54, 348 - 358, 2000.

[55] Masson-Delmotte, V., et al. *Holocene climatic changes in Greenland: Different deuterium excess signals at Greenland Ice Core Project (GRIP) and NorthGRIP*, J. Geophys. Res. vol. 110, D14102, 2005a.

[56] Masson-Delmotte, V., et al. *GRIP Deuterium Excess Reveals Rapid and Orbital-Scale Changes in Greenland Moisture Origin*, Science Vol. 309. no. 5731, pp. 118 - 121, 2005b.

[57] Marchal, O., et al. *Apparent long-term cooling of the sea surface in the northeast Atlantic and Mediterranean during the Holocene*, Quat. Sci. Rev., 21, 455 - 483, 2002.

[58] Mellor, G. L., and Yamada, T. *Developement of turbolence closure models for planetary boundary layers*, J. Atmos. Science, Vol. 31. pp. 1791 - 1806, 1982.

[59] Messinger, F., and Arakawa, A. *Numerical methods used in atmospheric models*, GARP Publication series 17, 1976.

[60] Metcalf, M., and Reid, J. *Fortran 90/95 explained*, 2nd edition, Oxford University Press, 1999.

[61] Hays, John Imbrie, J. D. and Shackleton, N. J. *Variations in the Earth's Orbit: Pacemaker of the Ice Ages*, Science vol. 194, number 4270, pp. 1121 - 1132, 1976.

[62] Marshall, J. and F. Molteni, 1993 *Toward a dynamic understanding of planetary-scale flow regimes*, J. Atmos. Sci. 50, 1792 - 1818, 1993.

[63] NGRIP members *High-resolution record of Northern Hemisphere climate extending into the last interglacial period*, Nature, 432, 147 - 151, 2004.

[64] Opsteegh, J. D., Haarsma, R. J., Selten, F. M. and Kattenberg, A. *ECBILT: A dynamic alternative to mixed boundary conditions in ocean models*, Tellus 50A, pp. 348 - 367, 1998.

[65] Pedlosky, J. *Ocean Circulation Theory*, 2nd edition, Springer-Verlag, 1998.

[66] Petit, J. R., et al. *Climate and atmospheric history of the past 420,000 years from the Vostok ice core, Antarctica*, Nature, vol. 399, no. 6735, pp. 429 - 436, 1999.

[67] V. Petoukhov, M. Claussen, A. Berger, M. Crucifix, M. Eby, A. V. Eliseev, T. Fichefet, A. Ganopolski, H. Goosse, I. Kamenkovich, I. I. Mokhov, M. Montoya, L. A. Mysak, A. Sokolov, P. Stone, Z. Wang and A. J. Weaver *EMIC Intercomparison Project (EMIPÛCO2): comparative analysis of EMIC simulations of climate, and of equilibrium and transient responses to atmospheric CO2 doubling* Climate Dynamics (2005) 25, 363 - 385, 2005.

[68] Renssen, H., Goosse, H., Fichefet, T. and Campin, J.-M. *The 8.2 kyr BP event simulated by a global atmosphere-sea-ice-ocean model* Geophys. Res. Lett., 28(8), 1567 - 1570, 2001.

[69] H. Renssen,1 H. Goosse, and T. Fichefet *Modeling the effect of freshwater pulses on the early Holocene climate: The influence of high-frequency climate variability*, Paleoceanography, vol. 17, no. 2, 2002.

[70] Renssen, H., et al. *Simulating the Holocene climate evolution at northern high latitudes using a coupled atmosphere-sea ice-ocean-vegetation model*, Climate Dynamics Volume 24, Number 1, 2005.

[71] Rimbu, N., et al. *Arctic / North Atlantic Oscillation signature in Holocene sea surface temperature trends as obtained from alkenone data*, Geophys. Res. Lett., 30(6), 1280, 2003.

[72] Rohling, E. J. and Pälike, H. *Centennial-scale climate cooling with a sudden cold event around 8,200 years ago*, Nature, vol. 434, pp. 975 - 979, 2005.

[73] Ruddiman, W. F., and McIntyre, A. *The mode and mechanism of the last deglaciation: Oceanic evidence*, Quat. Res., 16, 125 - 134, 1981.

[74] Sellers, W. D. *A global climatic model based on the energy balance of the earth-atmosphere system* Journal of Applied Meteorology, vol. 8, Issue 3, pp.392 - 400, 1969.

[75] Selten, F., M. *On the response of ECBilt-CLIO to increasing GHG concentrations*, Available at `http://www.knmi.nl/onderzk/CKO/ecbilt.html`

[76] Shaffer, G. and Sarmiento, J. L. *Biogeochemical cycling in the global ocean. I: A new, analytical model with continuous vertical resolution and high-latitude dynamics*, Journal of Geophysical Research, vol. 100, pp. 2659 - 2672, 1995.

[77] Steffensen, J. P. et al. *High-Resolution Greenland Ice Core Data Show Abrupt Climate Change Happens in Few Years* Science, vol 321, 680 - 683, 2008.

[78] Stocker, T. F., and Johnsen, S. J. *A minimum thermodynamic model for the bipolar seesaw*, Paleoceanography, vol. 18, no. 4, 2003.

[79] R. J. Stouffer, J. Yin, J. M. Gregory, K. W. Dixon, M. J. Spelman, W. Hurlin, A. J. Weaver, M. Eby, G. M. Flato, H. Hasumi, A. Hu, J. H. Jungclaus, I. V. Kamenkovich, A. Levermann, M. Montoya, S. Murakami, S. Nawrath, A. Oka, W. R. Peltier, D. Y. Robitaille, A. Sokolov, G. Vettoretti, and S. L. Weber *Investigating the Causes of the Response of the Thermohaline Circulation to Past and Future Climate Changes* Journal of Climate, vol. 19, pp 1364 - 1387, 2006.

[80] Thomasa, E. R., Wolff, E. W., Mulvaney, R., Steffensen, J. P., Johnsen, S. J., Arrowsmith, C., Whited, J., Vaughn, B., and Popp, T. *The 8.2 ka event from Greenland ice cores* Quaternary Science Reviews 26, 70 - 81, 2007.

[81] von Grafenstein, U., Erlenkeuser, H., Müller, J., Jouzel, J., Johnsen, S. *The cold event 8200 years ago documented in oxygen isotope records of precipitation in Europe and Greenland*, Climate Dynamics, 14 : 73D81, 1998.

[82] Wang, X. *Description of parameter control and output control for the atmosphere-ocean-sea-ice model*, Scientific Report, version 2, 2008.

[83] Woodruff, S. D., Slutz, R. J., Jenne, R. L., and Steurer, P. M. *A comprehensive ocean-atmosphere dataset*, Bull. Amer. Meteor. Soc. 68, 1239 - 1250, 1987.

[84] Wunsch, C. *What Is the Thermohaline Circulation?*, Science, vol. 298, 1179 - 1181, 2002.

[85] Xie, P. and Arkin, P. A. *Global Precipitation: A 17-Year Monthly Analysis Based on Gauge Observations, Satellite Estimates, and Numerical Model Outputs*, Bulletin of the American Meteorological Society, vol. 78, no. 11, 1997.